Supramolecular Organization of Polymeric Materials in Nanoporous Hard Templates

Martin Steinhart

Max Planck Institute of Microstructure Physics, Weinberg 2, 06120 Halle, Germany
steinhart@mpi-halle.de

Abstract A broad range of polymeric materials can be formed into nanotubes by means of nanoporous hard templates containing arrays of aligned, cylindrical nanopores. Functional hybrid membranes consisting of the nanoporous matrix and the nanotubes as well as released arrays of aligned nanotubes are thus accessible. The mechanical, chemical, optical, and electronic properties of the nanotubes as well as their specific surface are largely determined by the supramolecular organization of the material they consist of, and only the rational design of their internal morphology will pave the pay for their use as functional device components. Herein, recent efforts to tailor the mesoscopic structure of nanotubes by controlling the way precursors and target materials are deposited into the nanopores are reviewed. Moreover, specific attention is directed to structure formation processes such as crystallization, phase separation and mesophase formation under the influence of the two-dimensional confinement imposed by the pore geometry and the interfacial interactions with the pore walls. Nanoporous hard templates are particularly suitable for the rational generation of mesocopic fine structures in nanofibers because equilibrium and non-equilibrium states as well as unprecedented confinement-induced morphologies with new and exciting properties can be realized.

Abbreviations

AAO	Anodic aluminum oxide
BCP	Block copolymer
DMF	Dimethylformamide
D_p	Pore diameter
DSC	Differential scanning calorimetry
IR	Infrared
HA	Hard anodization
HRTEM	High-resolution transmission electron microscopy
L_0	Bulk period of a BCP
LC	Liquid crystal
MA	Mild anodization
M_W	Weight-average molecular weight
NMR	Nuclear magnetic resonance
Pluronic F-127	Ethyleneoxide$_{106}$-propyleneoxide$_{70}$-ethyleneoxide$_{106}$
PAN	Poly(acrylonitrile)
Pd	Palladium
PC	Polycarbonate
PDMS	Poly(dimethylsiloxane)
PE	Poly(ethylene)
PEO	Poly(ethylene oxide)
PL	Photoluminescence
PLA	Poly(lactide)
PMMA	Poly(methyl methacrylate)
PPO	Poly(propylene oxide)
PS	Poly(styrene)
PS-*b*-PBD	Poly(styrene-*block*-butadiene)
PS-*b*-PMMA	Poly(styrene-*block*-methyl methacrylate)
Pt	Platinum
PVDF	Poly(vinylidene difluoride)
SAED	Selected-area electron diffraction
SAXS	Small-angle X-ray scattering
SEM	Scanning electron microscopy
TEM	Transmission electron microscopy
TEOS	Tetraethoxysilane
T_c	Crystallization temperature
THF	Tetrahydrofuran
T_M	Melting temperature
T_p	Pore depth
WAXS	Wide angle X-ray scattering

1
Introduction

The range of materials that can be formed into nanotubes has been significantly extended during the past decade. However, it is still a challenge to

tailor the internal fine structure of the nanotube walls by controlling structure formation processes such as crystallization, mesophase formation and phase separation. The self-organization of the material the nanotube walls consist of on the supramolecular scale largely determines the chemical as well as the physical properties of the nanotubes and therefore their potential for real-life applications. For example, crystal size and crystal orientation in the walls of nanotubes consisting of semicrystalline polymers will largely influence their optical, electronic, mechanical and ferroelectric properties. As discussed below, mesoporous nanofibers that contain arrays of aligned cylindrical pores or hollow spaces with non-conventional geometries, such as helical pores, can be produced by the self-assembly of molecular block copolymer (BCP) soft templates under varying degrees of geometric confinement. The emerging interest in such "complex" nanotubes suggests that the traditional distinction between "nanotubes" and "nanorods" is somewhat arbitrary, if not obsolete. On the contrary, the design of the mesoscopic, supramolecular constitution of the one-dimensional nanostructures appears to be by far more crucial for their properties than the presence or absence of a hollow space in their interior. It is therefore highly desirable to control the formation of the internal morphology during the preparation of the nanotubes as far as possible.

Two fundamentally different strategies, both of which are associated with certain advantages and drawbacks, allow fabricating nanotubes of virtually any functional material. The first strategy, which is addressed in other parts of this volume, involves the direct self-assembly of molecular and supramolecular building blocks, or the use of soft templates that direct the formation of tubular structures from specific target materials or precursors thereof. The experimental configuration is simple because all components required for the synthesis are contained in one and the same solution, and self-assembly resulting in the formation of nanotubes often takes place under mild conditions. The nanotubes can be produced in large quantities, and their separation as well as their purification is possible with common methods such as filtration and centrifugation. However, the target materials the nanotubes consist of (or the corresponding precursors) must exhibit an intrinsic ability to self-assemble or they must interact with a structure-directing soft template in a very specific way. The range of materials that show these properties is limited. Moreover, it is difficult to arrange the nanotubes thus obtained into ordered arrays, as required for their integration into functional device architectures.

A complementary approach to the fabrication of nanotubes involves the use of hard templates as tools. Hard templates are either nanofibers or porous host materials. In the former case, the nanofibers are at first coated with the wall material of the tubes or a corresponding precursor. Subsequently, the template fiber, that is, the core of the hybrid fiber thus obtained, is selectively removed so that a shell of the material initially deposited onto the template nanofiber is conserved. Template fibers can, for example, be produced in high

quantities and with high aspect ratios (ratio of length and diameter) by electrospinning. Consequently, their use as templates makes non-woven fabrics consisting of nanotubes with high aspect ratios accessible, which are highly interesting materials for packaging, thermal insulation, storage, separation and high-performance filters [1].

However, if arrays of aligned nanotubes with precisely adjustable aspect ratios are required, nanoporous host materials exhibiting arrays of aligned nanochannels are the template of choice. Several kinds of nanoporous membranes [2] have been used as shape-defining molds, predominantly track-etch membranes and nanoporous anodic aluminum oxide (AAO), which can therefore be referred to as hard templates. Their use yields tubular structures from a broad range of polymeric materials, whose arrangement is determined by that of the pores in the hard template. The material the nanotubes consist of can directly be deposited onto the pore walls. It is also possible to infiltrate precursors or monomers into the nanoporous hard templates and to convert them into the target materials. A comprehensive body of literature, including many excellent review articles, deals with this topic [3–5]. The preparation of nanotubes inside the pores of nanoporous hard templates, which was pioneered by Martin and co-workers [6–14], automatically yields porous hybrid membranes whose channels are functionalized with the nanotubes in their interior. Examples for this are DNA-functionalized nanotube membranes with single-base mismatch selectivity [15] or membranes for enantioselective separations [16]. A problem associated with the fabrication of nanotubes by means of hard templates is the required availability of the latter. The release of the nanotubes is commonly achieved by a wet-chemical etching step destroying the hard template, which is a drawback for the up-scaling of template-based approaches to the fabrication of nanotubes. If they are attached to a support, they form more or less ordered arrays. Such arrays are of interest since they may exhibit specific wetting and adhesive properties [17, 18]. Recently reported approaches to the mechanical extraction of fiber arrays from porous templates [19, 20] need to be optimized and require that the nanotubes are tightly connected with an underlying substrate.

Despite these still-challenging issues, the fabrication of nanotubes using nanoporous hard templates is associated with several advantages beyond the possibility to align them. Readily available porous hosts such as self-ordered porous AAO have a narrow pore diameter (D_p) distribution and pores with D_p-values ranging from about 20 nm up to a few 100 nm. The pore depths (T_p) can be adjusted to values between about 1 μm and several 100 μm. Therefore, it is easily possible to tailor the diameter and the aspect ratio of the nanotubes. However, the most important advantage is the possibility to control mesoscopic structure formation processes inside the pores. There are relatively few limitations regarding the materials that can be formed into nanotubes via hard templates. Mixtures, sols, semicrys-

talline and liquid-crystalline polymers, other thermoplastics, as well as BCPs, are eligible for this approach so that the mesoscopic structure formation processes these materials undergo, such as phase separation, crystallization and mesophase formation, can be exploited to rationally generate specific, self-assembled supramolecular architectures in the tube walls. The degree of geometric confinement can be adjusted by the D_p-value. The chemical properties of the rigid pore walls of the hard template can by modified too, for example, by silanization or atomic layer deposition [21, 22]. The high surface-to-volume ratio of the nanoporous hard templates makes it possible to control self-assembly processes by adjusting the properties of the pore walls. This is particularly the case for self-assembly processes based on phase separation, as discussed below. Moreover, the walls of the template pores can be functionalized in such a way that they are electrically charged, a prerequisite for the fabrication of nanotubes by layer-by-layer deposition of polyelectrolytes. As common hard templates consist of inorganic materials such as alumina, they are stable at temperatures at which molten polymers are typically processed. There are no limitations regarding the temperature profile applied to the samples, that is, molten polymers can be crystallized either isothermally or non-isothermally. Hence, using hard templates in the synthesis of nanotubes is associated with various handles to tailor the internal fine structure of their walls.

The organization herein is as follows. Commonly used hard template systems will be described in Sect. 2. Section 3 deals with the infiltration of the target materials the nanotubes consist of or corresponding precursors into the pores. This step is far from being trivial. Even though the underlying physico-chemical phenomena are not completely understood, a qualitative overview of the infiltration mechanisms will be given. Crystallization and the formation of mesophases from liquid-crystalline molecular building blocks are important examples of self-organization processes of single-component materials that can be exploited to generate textured nanofibers (Sect. 4). As discussed below, not only the confinement but also the presence or absence of a bulk reservoir that is connected with the nanofibers influences the crystallization of polymers, which form lamella crystals and spherulitic superstructures in the bulk, inside the nanopores of hard templates. The texture in liquid-crystalline pore walls is the result of a delicate interplay of the anchoring to the pore walls and the growth kinetics. The exploitation of self-organization processes based on phase separation is discussed in Sect. 5. This includes the generation of fine structures by spinodal decomposition of mixtures as well as the formation of "complex" nanotubes and nanofibers with non-conventional morphologies by self-assembling BCPs inside the template pores. In this connection, we will also cover the synthesis of mesoporous nanofibers consisting of silica and amorphous carbon, as the underlying self-assembly processes are largely related to the BCP soft templates used as structure-directing agents. Section 6 deals with the preparation of nanotubes

by layer-by-layer deposition of polyelectrolytes and other polymeric materials into nanoporous hard templates. This technique involves the successive deposition of different target materials onto the pore walls, taking advantage of specific interactions between the species to be deposited and the already deposited layers. Thus, nanotubes having walls with a well-defined multilayer structure are accessible. This methodology also allows fabricating nanotubes composed of complex macromolecules such as dendrimeric polyelectrolytes and the controlled incorporation of nanoparticles such as luminescent quantum dots into the nanotube walls.

2
Hard Templates

A prerequisite for the template-based production of one-dimensional nanostructures and the rational exploitation of self-assembly processes in the two-dimensional confinement imposed by the pore geometry is the availability of suitable hard templates. In this section, a brief overview of commonly used hard templates, of their advantages and of their disadvantages will be given. However, it is beyond the scope of this contribution to exhaustively review the fabrication and properties of these porous materials. Commonly, two types of hard templates, both of which can contain arrays of aligned cylindrical channels as well as more complex pore shapes, are employed in the production of nanotubes and nanorods: track-etch polymer membranes and nanoporous AAO. Track-etch membranes [23, 24] (Fig. 1) are produced by irradiating polymeric films with a thickness ranging from a few microns to a few tens of microns with ion beams, thus producing latent tracks penetrating through the bombarded films. In a second step, pores are generated at the positions of the latent tracks by wet-chemical etching. Pore size, shape and density can be varied in a controllable manner by the proper selection of the conditions under which irradiation and post-treatment procedures are carried out. Pores with D_p-values ranging from 10 nm to the micron range are
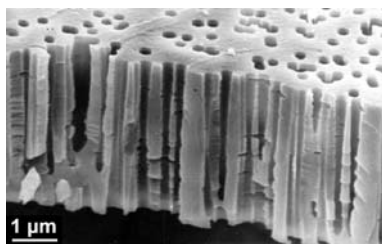

Fig. 1 Example of a polymeric track-etch membrane. Reproduced from [23]. © (2001) Elsevier

obtained, whereas the pore density can be adjusted to any value between 1 to 10^{10} pores per centimeter. Moreover, D_p-value and pore density can be adjusted independently. The most common polymers track-etch membranes consist of are polycarbonate and polyethylene terephthalate. The pore walls are commonly hydrophilized by plasma treatment or by adsorbing or grafting hydrophilic polymers, such as polyvinyl pyrrolidone, onto the pore walls. The limitations associated with track-etch membranes are their limited stability at elevated temperatures and their poor resistance against organic solvents, which poses problems for many of the self-assembly processes discussed below. The arrangement of the pores is random, that is, track-etch membranes do not exhibit long-range order. Moreover, because of their poor rigidity and their lack of chemical resistance to organic solvents, it is difficult to remove residual material from the surface of track-etch membranes after their infiltration, a process step that is crucial to the template-based fabrication of nanotubes and nanorods. Nevertheless, because of their commercial availability and versatility, track-etch membranes are being routinely used for the production of one-dimensional nanostructures. However, it was found that the pronounced roughness of the pore walls in track-etch membranes revealed by SEM and adsorption experiments prevents uniform orientation of anisotropic species infiltrated into the pores [24].

The second common hard template is nanoporous AAO with hydroxyl-terminated pore walls produced by the electrochemical anodization of aluminum substrates. From a practical viewpoint AAO has several advantages. It is stable at temperatures at which soft matter is commonly processed and resistant against organic solvents but can be selectively etched with aqueous acids and bases to release nanofibers fabricated inside its pores. The basis for the production of AAO is the well-known formation of porous oxide layers, whose thickness increases linearly with the anodization time, on bulk aluminum. To this end, electrolyte solutions are used that partially dissolve the freshly formed alumina [25–27]. At first, a homogeneous barrier oxide layer is generated on the aluminum substrate. Field-enhanced dissolution of the oxide occurs at fluctuations in the oxide layer, which leads in turn to the formation of pores. As the pore density increases, an array of pores characterized by a mean interpore distance develops. A stationary state in which pore growth is characterized by an interplay of field-enhanced dissolution of alumina at the pore bottoms and the formation of new alumina leads to stable pore growth [28, 29]. In AAO prepared under so-called mild anodization (MA) conditions, the amorphous pore walls consist of an outer layer containing water, electrolyte anions and positively charged defects, and an inner layer consisting of pure alumina [28]. The concentration profile of these contaminations across the pore walls is inhomogeneous (see, for example [30–32]). Even though it was shown that the pore walls of AAO hard templates are reactive at elevated temperatures of about 500 °C and above [33–35], in the temperature range relevant to the structure formation

of soft matter AAO hard templates can be regarded as inert, shape-defining molds.

Disordered, about 60 μm thick AAO membranes with a mean D_p-value of the order of 200 nm are commercially available (Whatman Anopore) [24]. These AAOs feature a broad pore size distribution as well as irregular pore shapes (Fig. 2a). The dispersity of the pore diameter distribution, calculated by dividing the standard deviation by the mean pore diameter, is typically larger than 20%. Initially, Anopore AAOs were designed as filters. Therefore, the nominal pore diameter refers to the narrowest pore segments that determine their separation performance. Moreover, the membrane surface of disordered AAOs exhibits pronounced roughness on different length scales that complicates the removal of residual material after infiltration and the purification of the nanostructures thus obtained.

The two-step MA process reported by Masuda and Fukuda involving self-ordered pore growth can be considered as a major breakthrough in AAO-based nanoprocessing [36]. A first anodization step is carried out in such a way that the initially disordered nanopores self-assemble into a hexagonal lattice. This uppermost alumina layer, the surface of which contains disordered pores, is removed by a selective wet-chemical etching step. The surface of the remaining aluminum substrate is patterned with hexagonal arrays of hemispherical indentations, which are replicas of the pore bottoms of the etched alumina layer. These indentations act as seeds for the growth of a hexagonal array of nanopores with T_p-values of up to several 100 μm in a second anodization step. Three self-ordered MA regimes have been identified. Using sulfuric acid as an electrolyte solution at an anodization voltage of about 25 V yields self-ordered AAO with a lattice constant of 65 nm and a D_p-value of about 25 nm [37]. Anodization with oxalic acid solutions at anodization voltages of about 40 V yields AAO with a lattice constant of 100 nm and a D_p-value of 35 nm [36], and anodization in phosphoric acid solutions at 195 V yields AAO with a lattice constant of 500 nm and a pore diameter of about 180 nm [38, 39]. The pores are arranged in hexagonal lattices charac-
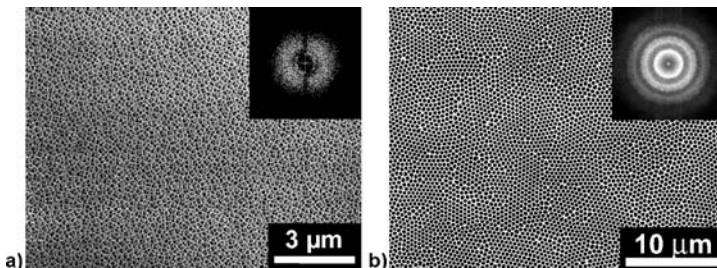

Fig. 2 Anodic aluminum oxide. **a** Example of disordered AAO with a mean D_p-value of 200 nm; **b** self-ordered AAO anodized with a phosphoric acid electrolyte solution under MA conditions. *Insets*: Fourier transforms

terized by a polycrystalline degree of order that consist of grains extending 10 to 20 lattice constants. The pore diameter distributions of self-ordered AAO have a dispersity of less than 8% and are therefore significantly sharper than those of disordered AAO. It was noted that the pore arrays produced in the self-ordering MA regimes exhibit a porosity of 10% [40]. Porosities up to 50% can be achieved if the pores are widened by isotropic wet-chemical etching (Fig. 2b). Self-ordered AAO produced by mild anodization is attached to underlying aluminum substrates and therefore mechanically stabilized. Moreover, the surface of self-ordered AAO is significantly smoother than that of disordered AAO. These two features substantially facilitate the fabrication, purification and characterization of nanoobjects prepared inside the pores of such hard templates, as well as the fabrication of functional membranes. Selective etching steps can be applied to remove the aluminum substrate and to open the pore bottoms.

MA requires several days of processing time and self-ordering pore growth occurs only in narrow process windows. Recently, the so-called hard anodization (HA), which is routinely being used in industrial processes, has been investigated as a new and complementary access to AAO hard templates. HA is performed at higher anodization voltages than MA, and the alumina layers grow orders of magnitude faster. Lee et al. reported that HA with oxalic acid solutions at anodization voltages between 120 and 150 V yields AAO with D_p-values of 49–59 nm and lattice constants of 220–300 nm,
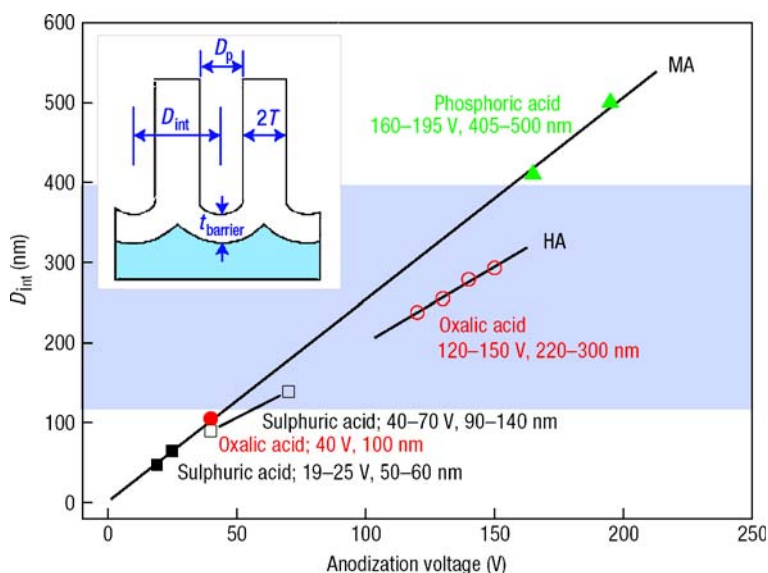

Fig. 3 Overview of currently identified self-ordering MA and HA regimes for the production of AAO. Reproduced from [41]. © (2006) Nature Publishing Group

a range not covered by the MA self-ordering regimes [41]. Moreover, the initial porosity of the HA membranes obtained with oxalic acid solutions lies in the range from 3.3 to 3.4% and is therefore significantly smaller than that of MA membranes. This is an important property of HA membranes that could enable the production of mechanically stable nanofiber arrays in which large distances between the nanofibers are required to prevent them from condensation. Recent efforts to conduct anodization of aluminum in sulfuric acid solutions under HA conditions to produce AAOs with lattice constants below 100 nm suffer from the poor mechanical stability of the AAOs thus obtained [42]. An overview of currently identified self-ordering MA and HA regimes is given in Fig. 3. Another important progress reported by Masuda and co-workers is the high-temperature anodization of aluminum in concentrated sulfuric acid solutions yielding self-ordered AAO with lattice constants as small as 30 nm and D_p-values of 18 nm [43, 44]. Long-range ordered AAO is accessible by combining self-ordering MA or HA regimes with lithographic prepatterning of the aluminum substrates used for anodization by means of hard-imprint lithography. However, this approach is limited to lattice constants larger than 100 nm because no master stamps with a smaller feature size are available [41, 45–47].

3
Nanotubes by Infiltrating Nanoporous Hard Templates

3.1
Wetting: Basic Concepts

The starting point for the fabrication of nanotubes by means of nanoporous hard templates is the infiltration of the target materials, of precursors thereof, or of monomers, into the pores. This process is far from being trivial and only partially understood. However, it is reasonable to assume that interfacial interactions dominate, or at least significantly influence both the infiltration and the mesoscopic structure formation. In the following, we will assume that exclusively physisorption occurs at the interface between the pore walls and the infiltrated material, neglecting the possibility of specific chemical interactions. In the literature it is often assumed that the filling of nanopores is driven by capillary action. As discussed below, this is only the case under certain conditions. To gain a qualitative understanding of the physico-chemical phenomena underlying the penetration of liquids into nanochannels, at first the well-investigated microscopic behavior of fluids deposited on smooth substrates will be discussed briefly. The surface energy of the substrate, the surface tension of the liquid, and the liquid/solid interfacial energy determine the macroscopic contact angle, at which a liquid/vapor interface meets the solid surface, according to Young's law [48]. The equilibrium contact angle is
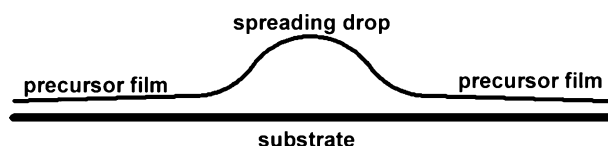
Fig. 4 Schematic diagram of a liquid drop spreading on a smooth substrate

a common measure of the wettability of a solid surface by a specific liquid. The system will adopt a state where the overall interfacial energy is minimized. A zero contact angle is equivalent to the spreading of the liquid, that is, to the maximization of the liquid/solid contact area. Commonly, polar inorganic surfaces exhibit high surface energies, whereas those of organic liquids and polymeric melts are about one order of magnitude lower [49]. Consequently, organic fluids commonly spread on inorganic, oxidic substrates. If the surface energies of the solid and the liquid converge, the contact angle will be larger than zero.

The question arises as to how a drop of a low-energy liquid spreads on a high-energy surface. Even for viscous polymeric fluids the formation of a precursor film could be evidenced [50–52]. At the foot of the drop, where the liquid contacts the solid surface, a thin film of the liquid emanates and covers large areas of the substrate (Fig. 4). In the proximity of the drop, the thickness of the film is in the mesoscopic range, whereas at the spreading front the film is thinner than a monolayer, as determined by ellipsometry, indicating an incomplete surface coverage. As the precursor film proceeds, the height of the macroscopic drop decreases. Taking into account that a finite amount of the fluid spreads on a surface large enough to be considered as "infinite", a "pancake" structure is nevertheless to be expected, that is, a liquid film covering a finite area with a thickness exceeding that of a monolayer. This is because the interactions between the solid and the liquid comprise attractive long-range interactions [53–55] expressed in terms of the so-called "disjoining pressure", that is, the pressure that has to be exerted to prevent the liquid film from thickening.

3.2
Precursor Wetting of Porous Templates with Polymeric Melts

When a fluid spreads on the walls of a nanochannel with a finite length, the situation is different from the spreading on smooth substrates in that the presence of an infinite bulk reservoir of the liquid can be assumed, whereas the solid surface to be wetted is finite. The infiltration of a liquid into an empty pore is qualitatively similar to the replacement of a liquid phase filling a cylindrical channel by another one having higher affinity to the walls of the channel. This process was intensively investigated theoretically and experimentally [56–59] because of its practical relevance to oil recovery from

bituminous sands, into which aqueous solutions are injected to replace and extract the oil. The underlying physics is complex and dependent on the dimensions of the channels hydrodynamic phenomena or interfacial phenomena dominate. In brief, at first a wetting film consisting of the liquid infiltrating the pores covers the pore walls (Fig. 5a). Instabilities in this film may occur (Fig. 5b), and as more and more liquid moves into the pores, these instabilities begin to grow until a "snap off" or "pinch off" takes place, that is, a meniscus forms (Fig. 5c). The interfaces of the meniscus move in opposite directions, and the pore volume is eventually completely filled with the liquid (Fig. 5d). It is reasonable to assume that the "snap-off" mechanism generally guides the infiltration of nanoporous and microporous materials with fluids.

If liquid, disordered polymers are brought into contact with porous hard templates exhibiting high surface energy and D_p-values significantly exceeding twice the radius of gyration of the infiltrated polymer, a polymeric precursor film with a thickness of a few tens of nanometers rapidly covers the entire area of the pore walls on a time scale of seconds to minutes even if the pores have a depth of the order of 100 micrometer. This behavior is commonly observed for AAO hard templates. Despite the fact that the pores should be completely filled in equilibrium, the liquid polymer layer is stable at least for several days. Consequently, polymer nanotubes can be obtained by solidifying the polymer [60–63]. For example, Fig. 6 shows a broken nanotube consisting of PS ($M_n \approx 850\,000$ g/mol) protruding from a self-ordered AAO template with a D_p-value of 400 nm and a T_p-value of 100 μm.

Up to now, the formation of mesoscopic polymer layers on the pore walls and the reasons for their kinetic stability are only qualitatively understood, if at all. It appears that the macromolecules have to be mobile enough to be removed from the bulk and to diffuse into the pores. Both entropic relaxation of the polymer chains and the disjoining pressure, as discussed in the
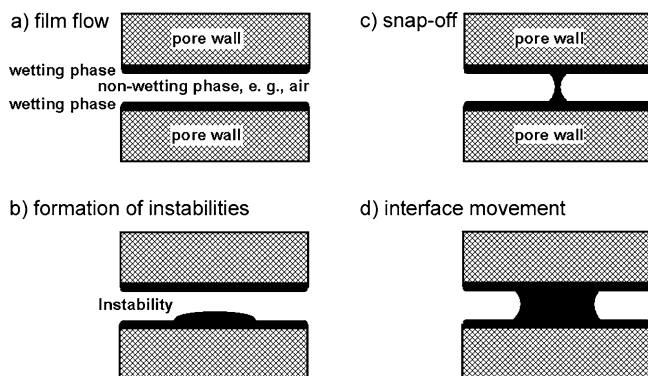

Fig. 5 Infiltration of a low molecular weight liquid (*black*) into a cylindrical channel
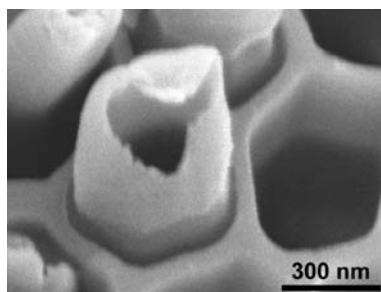
Fig. 6 PS tube prepared by precursor wetting protruding from an AAO hard template. Reproduced from [60]. © (2002) AAAS

previous section, may contribute to the generation of a polymer layer having a mesoscopic thickness. When the diameter of the pores in the hard template is reduced below about twice the radius of gyration of the infiltrated polymeric species, the hollow space in the tubes disappears and solid rods are obtained [64–67]. In general, precursor wetting takes place if the pore walls of the hard template exhibit high surface energy and if the polymeric melts are heated to temperatures well above their glass transition temperature [61, 68, 69]. However, many aspects of precursor wetting still need to be elucidated. Little is known about the relaxation processes leading to the formation of the mesoscopic polymer film, about the conformation of the polymeric chains in the nanotube walls, and about the parameters influencing the thickness of the nanotube walls.

3.3
Capillary Wetting of Porous Templates

If polymeric melts are infiltrated into nanoporous hard templates under conditions where the formation of a precursor film is suppressed, the filling of the pore volume is governed by classical capillarity, a mechanism that was intensively investigated in the context of capillary molding [70, 71]. The strong adhesive forces between the polymer and the pore walls are still effective but are not strong enough to drive single molecules out of the polymeric bulk reservoir on top of the hard template. However, removing single molecules from the bulk is a prerequisite for the rapid formation of a precursor film. In equilibrium, the overall interfacial energy is nevertheless minimized by completely filling the pore volume with the polymeric melt. To reach the equilibrium, a solid cylinder of the liquid but viscous polymer, preceded by a meniscus, slowly moves into the pores of the hard template [72] until the entire pore volume is filled. For example, Fig. 7a displays an array of nanofibers consisting of PS-b-PMMA infiltrated at 200 °C into an AAO membrane ($D_p = 400$ nm, $T_p = 100$ μm). The menisci of the nanofibers are clearly
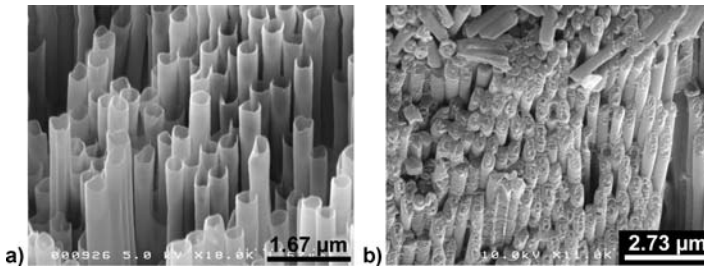
Fig. 7 PS-*b*-PMMA nanofibers prepared by capillary wetting into AAO hard templates. **a** Tips with menisci; **b** section through a PS-*b*-PMMA nanofiber array, evidencing the solid rod-like nature of the nanofibers. The SEM images are a courtesy Dr. Olaf Kriha

seen. The investigation of specimens containing fiber arrays cut along a plane slightly inclined with respect of the fiber axis reveals the solid nature of the fibers (Fig. 7b) [73].

The length of the fibers is proportional to the square root of the infiltration time, that is, the time the polymer is kept in the liquid state while in contact with the hard template [61, 72–74]. The time scale on which the pores are filled conveniently allows adjusting the length of the polymeric fibers by quenching the infiltrated polymer below its glass transition temperature or its crystallization temperature, respectively. For example, Moon and McCarthy could adjust the lengths of PS fibers prepared by melting PS ($M_W = 280\,000$ g/mol) at 200 °C in contact with an AAO membrane having a pore diameter of 200 nm to 0.6, 0.9, 1.2 and 1.6 μm by heating the polymer for 5, 10, 15 and 20 minutes, respectively [72]. Kriha et al. reported that loading a BCP melt with weight accelerated the infiltration, and that template pores ($D_p = 400$ nm) with a T_p-value of 100 μm were completely filled after 6 h [73].

Microphase-separated BCPs commonly fill the pores of hard templates via capillary wetting (Fig. 7) [73–75]. This is to be expected since the removal of single molecules from the bulk would disturb the ordered structure in the BCP. Moreover, the blocks had to diffuse (or to drift) through domains consisting of the other component. Thus, they had to overcome repulsive enthalpic interactions. In the case of disordered homopolymer melts, apparently a transition from precursor wetting to capillary wetting occurs that appears to be related to an increase in the viscosity of the polymeric melt, if hard templates having pore walls with a high surface energy are used. For example, PS ($M_n = 30\,500$ g/mol) forms solid rods in AAO membranes with a D_p-value of 200 nm after annealing for 2 h at 130 °C. However, increasing the infiltration temperature to 205 °C resulted in the instantaneous formation of nanotubes with lengths of 60 μm, corresponding to the T_p-value of the template pores [61]. She et al. observed that wetting AAO membranes having a D_p-value of 200 nm with polyamide 66 at 250 °C yielded nanowires [68].

Similar results were obtained for poly(propylene) [69]. Correspondingly, at a given infiltration temperature and for a given polymer, precursor wetting will occur if the molecular weight of the polymer is relatively low, whereas capillary wetting will occur in the case of relatively high molecular weights. For example, PS with a M_n-value of 30 500 g/mol forms nanotubes when infiltrated into AAO with a D_p-value of 200 nm at 205 °C, as discussed above. However, if the PS has a molecular weight of about 760 000 g/mol, again short nanorods where obtained [61]. It was suggested to exploit the dependence of the infiltration mechanism on the molecular weight for fractionating polymers with different molecular weights [61]. It should be noted that precursor wetting and capillary wetting represent only different kinetic routes to the equilibrium that is characterized by complete filling of the pores with the polymer. In the case of hard templates having pores with D_p-values of a few tens of nm, not only capillary wetting but also precursor wetting will yield solid nanorods, as discussed in the previous section. However, the rates at which the pores are filled with the polymer potentially allow for distinguishing between both mechanisms. Shin et al. reported a significantly enhanced mobility of polymer chains in very narrow pores having D_p-values smaller than the radius of gyration of the infiltrated polymer, a finding that was attributed to a confinement-induced decrease in the degree of intermolecular entanglement [76]. Because of the confinement imposed by the pore geometry, the chains are not stretched in the direction of flow but are compressed in a direction orthogonal to the flow. Consequently, it is reasonable to assume that the parameter that determines the wetting mechanism is the energetic and entropic effort required to remove the polymer chains from the bulk reservoir on top of the hard template and to draw them into the pores.

Combinations of both wetting mechanisms identified so far allow fabricating new and unprecedented one-dimensional nanostructures, for example, tube/rod hybrid fibers. To this end, AAO hard templates were infiltrated with BCPs under conditions of capillary wetting in such a way that pore segments with an adjustable length were filled with solid BCP rods. Then, the hard templates were turned upside down and a homopolymer was infiltrated from the reverse side under conditions of precursor wetting. The composite fibers thus obtained consisted of a stiffer, solid BCP segment and a more flexible, tubular homopolymer segment (Fig. 8) [73].

Another means to control the infiltration mechanism is the surface energy of the pore walls of the hard template. For example, Grimm et al. obtained short polymer rods with hard templates modified with a silane coupling agent bearing perfluorated organic moieties under conditions where otherwise tubes had formed [20]. Thus, the formation of a precursor film can be suppressed completely by reducing the surface energy of the hard template. However, under these conditions, the polymeric melt might not spread on
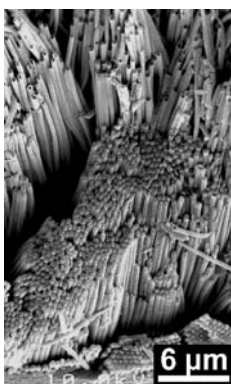
Fig. 8 Cross-sectional view of an array of tube/rod hybrid nanofibers obtained by infiltrating polymers into hard templates at first under conditions of capillary wetting and subsequently from the reverse side of the hard template under conditions of precursor wetting. Reproduced from [73]. © (2007) Wiley-VCH

the pore walls and external pressure has to be applied to inject the molten polymer into the pores.

3.4
Template Wetting with Polymeric Solutions

The infiltration of solutions consisting of a polymer and a volatile low molecular mass solvent into nanoporous hard templates has been intensively investigated [13, 65, 68, 69, 77–81]. In principle, it is sufficient to drop the solution onto the hard template and to let the solvent evaporate. However, it is far from being trivial to predict whether the properties of such a mixture rather correspond to those of a low-molecular mass liquid or to those of a polymeric melt. Two limiting cases can be postulated: If the solution at first completely fills the pore, the polymeric layer on the pore walls forms by adsorption from solution. In this case, the concentration of the polymer and the volume of the solution deposited on the hard template will certainly affect the formation of the polymeric nanostructures inside the pores. The solvent evaporates at the solvent/air interface so that the solution becomes more and more concentrated. The increasing concentration of the polymer will change the nature of the adsorbed polymer layer on the pore walls. Eventually, it will become important which portion of the polymer contained in the applied volume of the stock solution is still located on top of the hard template when the polymer solidifies as the solvent content drops. If the mixture behaves like a polymeric melt, it is to be expected that it will infiltrate the pores according to the precursor wetting mechanism since the solvent acts as a plasticizer. Then, a swollen mesoscopic polymer layer covers the pore walls. In any case, the evaporation of the solvent, a process that can hardly

be controlled in a satisfying manner, will influence the morphology of the polymeric nanostructures. Liquid/liquid phase separation [82, 83] and wetting transitions [84] may occur when the composition of the system changes. Moreover, evaporation may lead to a temporary concentration gradient inside the pores along with non-uniform vitrification [85]. Structure and density of the absorbed layer will not only strongly depend on the polymer/solvent interactions [86–88] but also on environmental conditions such as temperature and humidity. Little is known about the conformation of polymer chains covering the pore walls of hard templates infiltrated by polymeric solutions. Primak et al. studied PDMS films ($M_w = 10\,940$ g/mol) deposited from a solution in chloroform into AAO membranes by deuterium nuclear magnetic resonance spectroscopy [80]. They found a high degree of surface-induced ordering inconsistent with the expected loop/tail conformations and suggested that the chains in the proximity of the pore walls were flattened and that particularly strong interactions between the monolayer covering the pore walls and the pore walls were present. However, it remains unclear to what extent these findings are specific to the system investigated by these authors.

In contrast to the conformation of the polymer chains, the morphology of polymeric nanostructures can easily be probed by SEM and TEM. Ai et al. reported that nanotubes are obtained if diluted solutions of PS ($M_w = 270\,000$ g/mol) in cyclohexane infiltrate AAO membranes at 35 °C, that is, under θ-conditions, whereas infiltration of concentrated solutions results in the formation of solid rods [81]. This is in line with results reported by Song et al., according to which the wall thickness of PS nanotubes deposited from solutions in dichloromethane increased with increasing concentration of PS [77]. Chen et al. obtained amorphous carbon nanotubes by infiltration of solutions of PAN in DMF, crosslinking of the PAN and subsequent carbonization. Again, the walls of the so-obtained carbonaceous nanotubes were thicker for higher PAN concentrations in the infiltrated stock solutions. In this case, the wall thickness could also be tuned by performing successive infiltration-pyrolysis cycles [89]. However, it should be noted that infiltration of solutions into AAOs often results in the formation of short, defect–rich fiber segments [79].

Only few attempts have been made to rationally design the mesoscopic fine structure of nanotubes fabricated by wetting nanoporous hard templates with polymeric solutions. Chen et al. infiltrated solutions of PS-*b*-PAN in DMF into AAO. As described above, the PAN was at first crosslinked and then carbonized. However, the PS domains were converted into holes, and porous amorphous carbon nanotubes could be fabricated [89]. In a similar approach, Rodriguez et al. used a solution of PS-*b*-PVP and carbohydrates associated with the PVP blocks via hydrogen bonds in DMF into AAO and obtained mesoporous amorphous carbon nanotubes with the positions of the mesopores determined by the positions of the PS domains. Solvent annealing of the BCP/hydrocarbon films in DMF/benzene vapor led to a significantly
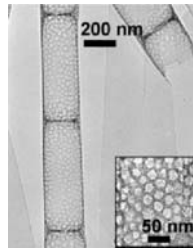
Fig. 9 TEM image of nanoporous carbonaceous nanotubes prepared using PS-*b*-P2VP with a bamboo-like structure. *Inset*: Hexagonal arrays of pores on the tube wall. Reproduced from [90]. © (2006) American Chemical Society

more uniform distribution of the PS domains and hence of the pores in the amorphous carbon nanotubes [90]. Apparently, in contrast to the infiltration of polymeric melts, tubular structures with walls consisting of BCPs can be obtained in this way. In both works, the hard AAO templates had a D_p-value of about 200 nm, and the occurrence of bamboo-like morphologies or ring-like ribs arranged more or less periodically along the nanotubes was reported (Fig. 9). Chen et al. attributed the formation of this structure to self-organization processes related to the evaporation of the solvent, similar to those reported by Gonuguntla and Sharma, who investigated the evaporation of an initially pure solvent drop on a smooth, dissolving polymer substrate [91].

An interesting self-ordering phenomenon is the occurrence of Rayleigh-Plateau instabilities. It is well known that annular liquid films are, similar to liquid cylindrical threads, susceptible to the growth of periodic thickness fluctuations [92, 93]. Chen et al. reported that nanotubes prepared by infiltrating AAO hard templates with 5 wt-% solutions of PMMA ($M_w = 22\,700$ g/mol) in chloroform can be converted into nanorods with periodic encapsulated holes driven by the Rayleigh instability [94]. At first, a smooth polymer film covered the pore walls. Thermal annealing of the PMMA/AAO hybrid membrane at temperatures above the glass transition temperature of the PMMA resulted in the growth of thickness undulations in the annular PMMA film and finally in the formation of bridges across the entire nanopore. The wavelength of the periodic structure increases with D_p and amounts to about 1000 nm for a D_p-value of 200 nm. Figure 10a shows a TEM image of a PMMA tube with periodically undulated pore walls, and Fig. 10b a TEM image of a hole-containing PMMA nanorod.

On the one hand, template wetting with polymeric solutions is, up to now, poorly understood and difficult to perform in a reproducible manner under well-defined conditions. On the other hand, solution wetting offers a plethora of possibilities to generate one-dimensional nanostructures exhibiting complex morphologies and fine structures. To this end, as discussed in Sect. 5, mixtures of functional materials or precursors thereof in a common solvent
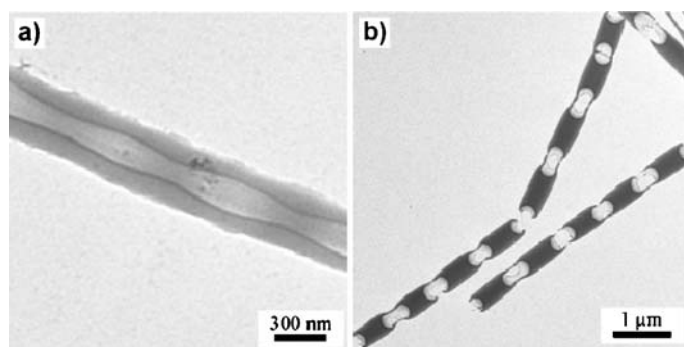
Fig. 10 Rayleigh instabilities in PMMA nanofibers. **a** TEM image of a PMMA tube with periodically undulated pore walls; **b** TEM image of a hole-containing PMMA nanorod. Reproduced from [94]. © (2007) American Chemical Society

can be infiltrated into hard templates to exploit phase separation processes inside the pores as a structure formation process.

4
Self-Assembly of Single-Component Materials in Nanopores

4.1
Overview

Crystallization and mesophase formation determine the optical, electronic, mechanical, chemical and piezoelectric properties of polymeric materials to a large extent. For example, supramolecular self-organization enhances charge transport in conjugated polymer semiconductors [95]. Also, the performance of stimuli-responsive materials may depend on their mesoscopic fine structure. Whereas in inorganic ferroelectrics slight dislocations within the crystalline unit cell lead to polarization switching, changing the orientation of the polar axis in ferroelectric polymers [96] is associated with rotations about C – C bonds in the backbone [97–99]. Consequently, the polar axis of the unit cells in ferroelectric polymer crystals can only adopt certain orientations which are coupled with the crystal orientation. It is, therefore, reasonable to assume that control over crystallization and mesophase formation inside hard templates is crucial to the rational design of one-dimensional nanostructures.

Little is known about the nature of disordered, amorphous interphases covering the pore walls of nanoporous hard templates, but a limited body of literature deals with ordered supramolecular architectures in single-component nanotubes and nanorods confined to hard templates. Mesoscopic morphologies characterized by a crystalline or liquid-crystalline degree

of order and by pronounced anisotropy can be generated by infiltration of semicrystalline or liquid-crystalline polymers as isotropic liquids and subsequent crystallization or mesophase formation inside the hard template pores. Common experimental techniques, including WAXS [64, 100], SAED [65, 101], HRTEM [102, 103], polarized IR spectroscopy [7, 10, 12, 101], and DSC [64, 100, 104] have been applied to characterize ordered supramolecular architectures in one-dimensional nanostructures. WAXS on ensembles of aligned nanofibers provides valuable information on textures, whereas SAED and HRTEM can be used to locally elucidate crystal orientations and to determine the polymorph formed. Whereas WAXS is easy and straightforward to apply on AAO membranes loaded with soft matter, electron microscopy in general suffers from strong interactions between the nanostructures being probed and the incident electron beam. This drawback may be overcome by short exposure times or by cooling the samples [65]. Up to now, SAXS is no established method for probing textures and mesoscopic features such as long periods in one-dimensional nanostructures. As long as they are aligned within the templates, the background scattering of the matrix material may pose problems for the evaluation of the SAXS patterns, and in the case of released nanofibers the inhomogeneous nature of the powders used for performing SAXS experiments hampers the analysis of the collected data. Much information can be gained by polarized IR spectroscopy [105]. On the one hand, it is often possible to assign specific peaks to amorphous and crystalline material so that the crystallinity can be deduced from the peak areas. On the other hand, anisotropy is obvious from infrared dichroism that is accessible by comparing peak areas in spectra taken with IR beams whose planes of polarization are inclined by specific angles. DSC yields information on the crystallization kinetics and nucleation mechanisms, as well as on crystal sizes. In principle, NMR and dielectric spectroscopy should also be applicable methods that have, up to now, virtually not been explored for the study of supramolecular architectures in nanoporous hard templates. However, at least for NMR, a proof of concept was reported by Primak et al. [80].

Mesoscopic structure formation processes inside hard templates can be influenced by surface-induced ordering and geometric confinement since their characteristic length scales are of the same order of magnitude as the D_p-values of the nanopores or the thickness of the nanotube walls they contain. Already early works on template syntheses of functional polymers by Martin and co-workers indicated that supramolecular order and properties such as conductivity may be enhanced inside hard templates [11]. Polypyrrole and poly(3-methylthiophene) [6], polyacetylene [7] and polyaniline [10] nanofibers having diameters in the mesoscopic range were obtained by synthesizing the corresponding polymers in the nanopores. Their enhanced conductivity, which was evidenced for nanofibers aligned in the hard templates and for mats consisting of released nanofibers [106] was attributed to en-

hanced supramolecular order [7, 11, 12, 107]. Polymerization within the pores involves preferential growth of the chains located on the pore walls of the hard template because of their reduced solubility as compared to the monomer. Therefore, after short polymerization times, the nanotubes thus formed predominantly consist of polymer chains in proximity to the pore walls, where they are aligned and the formation of kinks and bends is suppressed. Martin and co-workers therefore concluded that the enhanced supramolecular ordering thus realized is accompanied by an increased conjugation length, which in turn results in higher conductivity. This surface-induced alignment was found to decay when thicker nanotube walls were prepared by longer polymerization times.

4.2
Crystallization of Thermoplastics

One of the most important structure formation processes in polymeric materials having chain architectures that allow, at least to some extent, packing of the chains is crystallization. The crystallinity of semicrystalline polymers, as well as the morphology and the orientation of the crystalline entities, largely determine the properties of these materials. Polymers usually crystallize as lamellar crystals in which folded chains are oriented approximately perpendicular to the surface of the lamellae [108–110]. The typical thickness of these crystals lies in the nanometer range, while their lateral dimensions are in the micrometer range, thus by far exceeding typical D_p-values of hard templates. Within the crystals, the chains adopt a helical conformation, and the growth of the lamellae proceeds in the lateral directions. On a larger scale, the lamellae are organized in spherulites, densely branched, isotropic, polycrystalline superstructures [111–113]. It is an intriguing question as to how the geometric confinement of the pores in nanoporous hard templates and their large surface-to-volume ratio influences the crystallization of polymers. In the case of melt infiltration of semicrystalline polymers into hard templates, crystallization is an important issue because crystallization may occur upon cooling to room temperature. Even though, up to now, only a limited number of publications deals with this topic [64, 79, 100, 101, 104], it has become clear that crystallization of polymers confined to the pores of hard templates can be influenced, and to some extent engineered, by the presence or absence of a bulk polymer reservoir in contact with the polymer inside the pores, by the D_p-value of the hard template, and by the temperature profile applied.

Generally, the c-axis of the polymeric crystals, which is commonly normal to the plane of the lamella crystals, orients perpendicular to the pore axes. This enables the lamellae to grow along the pores. Moreover, the crystallinity of the material inside the pores is typically below that of the corresponding bulk material. In the case of non-isothermally crystallized PVDF, the crys-

tallographic direction exhibiting the highest growth rate, that is, the ⟨020⟩
direction, aligns with the pore axis, resulting in uniform crystal orientation
inside the pores on a macroscopic scale [79], if crystallization is initiated
by heterogeneous nucleation [114, 115] in a bulk PVDF reservoir on top of
the hard template. The lamellae in the spherulites in the bulk reservoir are
oriented in such a way that their direction of fastest growth points radially
outwards. If a growing spherulite hits the surface of a hard template infiltrated
with PVDF, only those lamellae proceed into the pores whose ⟨020⟩ direction
is, within a certain tolerance, oriented parallel to the pore axes [64]. If the
bulk reservoir is removed from the surface of the hard template, crystalliza-
tion in each crystallizing entity is predominantly initiated by homogeneous
nucleation at high supercooling, because the probability of the occurrence
of heterogeneous nuclei in the small volume of the nanopores is negligi-
ble. Then, crystals with one of the ⟨hk0⟩ directions aligned with the pore
axes, a crystal orientation that enables growth of the lamellae along the
pores, form with statistical frequency. This was evidenced by WAXS meas-
urements performed in $\Theta/2\Theta$ geometry on PVDF nanofibers aligned within
the pores of the hard templates, crystallized in the presence or absence of
a bulk PVDF reservoir. In the former case, only the (020) peak appears
in the XRD pattern (Fig. 11a), in the latter case all (hk0) peaks show up
(Fig. 11b) with relative intensities similar to those in the powder pattern of
isotropic PVDF (Fig. 11c). However, it is striking that reflections with non-
zero l-index are still missing in the pattern of the sample crystallized in
the absence of the bulk reservoir. This is because crystals with a corres-
ponding orientation impinge on the pore walls and therefore occupy only
a small portion of the pore volume. DSC cooling scans nicely confirmed
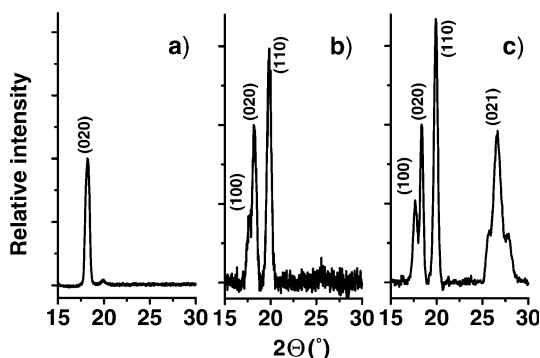that homogeneous nucleation significantly contributes to the crystallization

Fig. 11 WAXS patterns of PVDF nanofibers aligned in an AAO hard template (D_p = 35 nm)
measured in $\Theta/2\Theta$ geometry. **a** Non-isothermal crystallization in the presence of a bulk
PVDF surface reservoir; **b** non-isothermal crystallization in the absence of a bulk PVDF
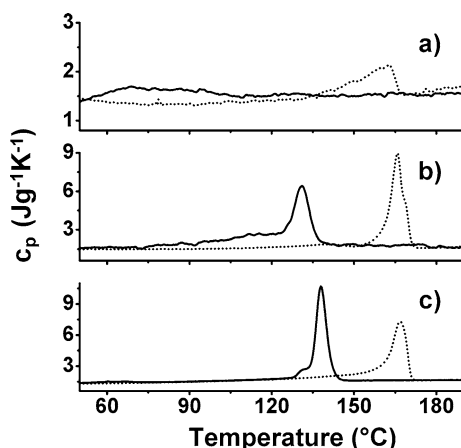surface reservoir; **c** powder pattern of an isotropic sample

Fig. 12 DSC scans of separated PVDF nanostructures within templates (*dotted curves*: heating runs; *solid curves*: cooling runs; heating and cooling rates: 20 K = min). **a** Nanorods (D_p = 35 nm); **b** nanotubes (D_p = 400 nm); **c** bulk PVDF. The *curves* were corrected by subtracting the contribution of the alumina (determined by reference measurements of empty templates). Reproduced from [64]. © (2006) American Physical Society

of an ensemble of separated PVDF nanotubes inside an AAO template with a D_p-value of 400 nm, whereas exclusively homogeneous nucleation occurs if the D_p-value is reduced to 35 nm (Fig. 12). Random PVDF copolymers with trifluoroethylene P(VDF-*ran*-TrFE) infiltrated into AAOs with D_p-values ranging from 55 to 360 nm were also investigated and found to be crystalline. By probing the relative permittivity of arrays of P(VDF-*ran*-TrFE) nanofibers the ferroelectric-to-paraelectric phase transition could be observed [66, 67].

Woo et al. investigated the crystallization kinetics of separated entities of linear PE inside AAO hard templates by DSC and came to the conclusion that inside pores with D_p-values below about 50 nm heterogeneous nucleation at the pore walls becomes dominant, whereas for D_p-values of 62 and 110 nm homogeneous nucleation initiates crystallization [104]. The Avrami constant n that depends on the growth geometry and the nucleation mechanism was found to be smaller in the case of PE crystallizing in the nanopores than for bulk crystallization, indicating that crystal growth inside the pores is frustrated and dominated by nucleation occurring at high supercooling. Plotting the reciprocal crystallization half time, that is, the crystallization time at which the crystallinity reaches half of the finally attained value at a given crystallization temperature, versus the crystallization temperature T_c and the supercooling, respectively, revealed that the crystallization rates for bulk samples depend on the degree of supercooling. This dependence was significantly more pronounced for PE confined to AAO hard templates hav-
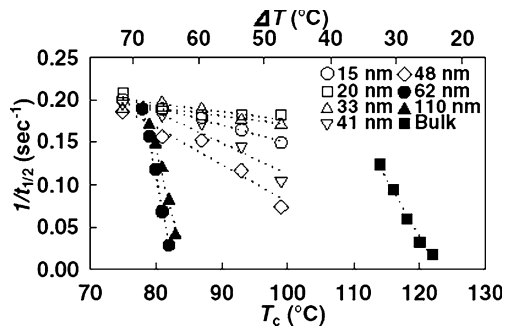
Fig. 13 Reciprocal of crystallization halftime ($1/t_{1/2}$) of PE confined to AAO with different D_p-values as a function of the crystallization temperature (T_c) and the degree-of-supercooling (ΔT). Reproduced from [104]. © (2007) American Physical Society

ing D_p-values of 110 and 62 nm. However, for D_p-values below 50 nm, only a weak dependence of the crystallization rate on the supercooling was found (Fig. 13), indicating the transition from dominant homogeneous nucleation in the larger pores to heterogeneous surface nucleation in the smaller pores. This transition was attributed to the fact that the smaller pores have a much larger surface-to-volume ratio, whereas the frustration of the crystal growth is more pronounced too.

A more detailed analysis of WAXS patterns of PE inside AAO hard templates revealed that, even though the ⟨110⟩ direction is being considered as the direction of fastest crystal growth, the *b*-axis aligns with the long axes of the template pores [100]. Whereas the orientation distribution of the crystals was found to be narrower in smaller pores, DSC melting runs also revealed a shift of the position of the melting endotherms to lower melting temperatures T_M along with smaller D_p-values. Consequently, the calculation of T_M using the Gibbs–Thomson equation, assuming that crystal growth is confined in three dimensions, yielded results fitting much better to the experimental values than T_M-values calculated assuming unlimited crystal growth along the pores. Also, the crystallinity decreased with decreasing D_p. Shin et al. concluded that crystal growth of PE along the pores is indeed restricted because the dominant growth direction of the crystals is not aligned with the long axes of the template pores.

Polarized IR spectroscopy was employed by Wu et al. to investigate crystallinity, the formation of different crystal orientations and the crystal texture of syndiotactic PS (sPS) crystallized inside AAO hard templates while in contact with a bulk reservoir of the same polymer [101]. The β-polymorph was obtained by cooling from the melt to 260 °C and crystallizing at this temperature for 2 h, while heating amorphous samples quenched from the molten state to 240 °C and heating to this temperature for 2 h resulted in the formation of the α-polymorph. A comparison of the areas of peaks
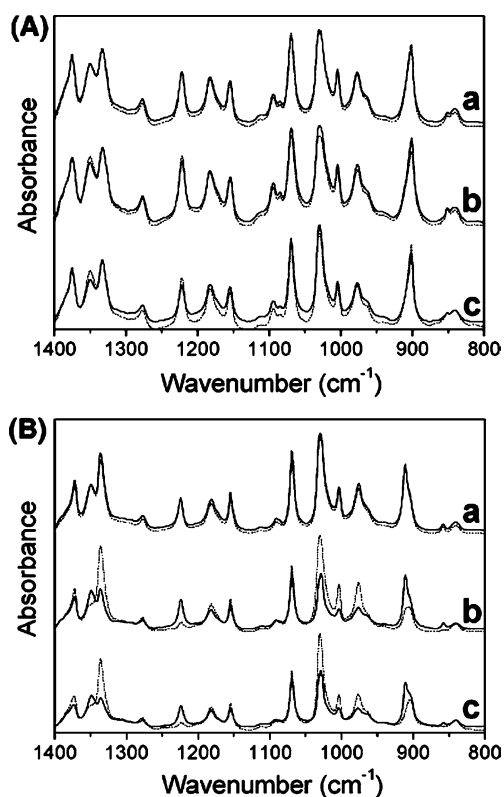
Fig. 14 Polarized infrared spectra of sPS crystallized at lower temperatures (**A**) and at 260 °C (**B**). (*a*) represents the bulk, (*b*) nanorods prepared inside AAO with D_p = 200 nm, and (*c*) nanorods prepared inside AAO with D_p = 80 nm. Polarization perpendicular to nanorod axes: *solid lines*; polarization parallel to nanorod axes: *dashed lines*. Reproduced from [101]. © (2007) American Chemical Society

characteristic of amorphous sPS and the β-polymorph revealed again a decreasing crystallinity along with decreasing D_p. For the bulk and D_p-values of 200 and 80 nm, crystallinities of 62.0, 49.8 and 36.2%, respectively, were obtained. The evaluation of polarized IR spectra measured on bulk sPS and sPS confined to AAOs with D_p-values of 200 and 80 nm (Fig. 14) revealed that samples crystallized at 240 °C consisting of the α-polymorph were isotropic. In samples crystallized at 260 °C consisting of the β-polymorph no preferred orientation of bulk sPS was observed, whereas inside the AAO hard templates the *c*-axes in the crystals and thus the chain axes were oriented perpendicular to the pore axes. The apparent differences in the degree of crystal orientation in the AAO/sPS hybrid samples were attributed to the different thermal histories. The α-polymorph was obtained by heating quenched amorphous samples from low temperatures to the target crystal-

lization temperature of 240 °C. Therefore, a temperature range was passed that is characterized by a high nucleation rate at high supercooling. Therefore, crystallization was governed by nucleation, and because of the presence of many small growing crystallites no texture could develop. However, the β-polymorph was obtained by cooling from the isotropic melt in contact with a bulk reservoir. Then, it is to be expected that crystallization is initiated by a small number of heterogeneous nuclei so that crystallization is dominated rather by crystal growth than by nucleation. Consequently, crystals having a major growth direction oriented parallel to the pore axes dominate.

O'Carroll et al. infiltrated molten poly(9,9-dioctylfluorene) (PFO) at 250 °C into AAO membranes and obtained solid nanorods consisting of this polymer [116]. As compared to the bulk PL spectrum, a red-shift of the peaks along with an enhanced vibronic structure was found in the PL spectrum of the nanorods, indicating a narrowed orientation distribution of the emitting chain segments accompanied by an increased effective conjugation length. It is noteworthy that this observation was made on solid nanowires, whereas for nanotubes consisting of conducting polymers obtained by polymerization in hard templates only the polymer layers in the proximity of the pore walls exhibited enhanced ordering, as discussed in Sect. 4.1 [11]. The PFO nanorods exhibited waveguide behavior, as demonstrated by local excitation of nanorod segments away from the tip and by simultaneously probing the light emission at the tip by PL microscopy. Evaluation of the intensity of the emission at the nanowire tip as a function of the propagation length revealed the occurrence of propagation losses that significantly increase with increasing distance between the excitation spot and the nanorod tip. The analysis of spatially resolved PL spectra of the waveguided emission at the nanorod tip revealed that the attenuation of shorter-wavelength peaks was stronger than that of longer-wavelength peaks, a finding that was attributed to reabsorption. However, Rayleigh scattering resulting from density fluctuations in the waveguide material on length scales one to two orders of magnitude shorter than the wavelength of the propagating light apparently contributed to the observed losses in a significant manner. The presence of such fluctuations giving rise to local variations in the refractive index along the nanorods was visualized by dark-field TEM, revealing that the nanorods contain some crystallites with diameters of a few tens of nm with orientations deviating from that of the matrix.

These results suggest that a careful and precise engineering of the crystalline morphology in one-dimensional nanostructures consisting of semicrystalline polymers is indispensable for the optimization of their performance as device components in real-life applications. Furthermore, the investigation of the crystallization in polymeric nanotubes and nanorods aligned in the nanopores of rigid hard templates is complementary to studies on the crystallization of semicrystalline blocks in microphase-separated

BCPs [117–121]. The concepts discussed above may help to understand the crystallization behavior of bulk polymers as well as that of non-polymeric materials such as pharmaceuticals [122] and inorganic semiconductors [123] confined to nanoporous hard templates.

4.3
Columnar Mesophases

Besides the exploitation of melt crystallization in thermoplastics, the formation of ordered assemblies consisting of molecules having an anisotropic shape is a self-assembly process with great potential for the fabrication of nanotubes with a customized mesoscopic fine structure inside the pores of hard templates. To this end, particularly disc-like molecules that self-organize into columnar stacks, so-called discotics [124], are promising building blocks. For their anchoring to the surface of a substrate, two limiting cases can be formulated. "Edge-on" orientation means that the molecular planes are oriented normal to the surface of the substrate. The columns formed by the disk-shaped molecules then have a so-called "planar" orientation. "Face-on" anchoring means that the molecular planes are parallel to the substrate surface. Then, the orientation of the columns is called "homeotropic" (Fig. 15). The way how the discs assemble on a surface depends on the intercolumnar interactions between adjacent discs and the interactions between the disks and the substrate.

Particularly polycyclic aromatic hydrocarbons (PAHs) [126] have attracted considerable interest, because their pyrolysis yields nanotubes whose walls consist of graphene layers. For example, Zhi et al. deposited disc-like PAHs of the hexa-*peri*-hexabenzocoronene (HBC) type into AAO hard templates from solutions in dichloromethane [103]. The discs were anchored edge-on, and columns with a planar orientation with respect to the pore walls formed, driven by strong $\pi-\pi$ interactions between the HBC discs. Subsequent pyrolysis yielded nanotubes whose walls consisted of highly ordered graphene
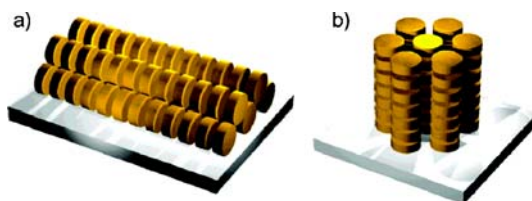

Fig. 15 Schematic representation of the different types of supramolecular arrangements of discotics on surfaces with **a** edge-on orientation of the molecules, where the columnar axis is oriented parallel to the substrate (planar texture), and **b** face-on arrangement of the discotics leading to a homeotropic texture. Reproduced from [125]. © (2005) Wiley-VCH

layers oriented perpendicular to the tube axes. Therefore, the initial orientation of the HBC precursors was conserved during the carbonization step. The properties of the HBC molecules can be engineered by modifying the substitution pattern at the polycyclic aromatic core. Long, branched alkyl side chains as substituents lead to low isotropization temperatures so that melts of correspondingly designed HBC molecules could be infiltrated into AAO hard templates [127]. In this case, the discs formed columns oriented planar with respect to the pore walls in which the plane of the disks was inclined by 45° with respect to the column axis and the long axes of the template pores. HBC molecules bearing acrylate units at the end of six alkyl spacers attached to the polycyclic aromatic core were synthesized by Kastler et al. [128]. The HBC molecules thus modified can easily be cross-linked via the acrylate functions. Deposition of these HBC discs from a solution in dichloromethane into AAO hard templates led to the formation of nanotubes whose walls consisted of long-range ordered stacks of crosslinked HBC molecules aligned with the nanotube axes. Apparently, the discs were anchored edge-on to the pore walls. Cross-linking at a moderate temperature of 170 °C fixated the supramolecular columnar architecture without destroying the polycyclic aromatic core of the molecule. The nanotubes thus obtained therefore exhibited high mechanical stability, whereas the supramolecular order, the formation of which had been driven by π–π interactions between the HBC discs, was conserved as revealed by HRTEM and SAED (Fig. 16). In the case of hyperbranched tetraphenylcyclopentadienone building blocks deposited from solutions in dichloromethane, crosslinking by a Diels–Alder reaction fixated the supramolecular architecture, and stable tubular nanostructures were obtained. Subsequent carbonization yielded carbonaceous nanotubes exhibiting a highly porous fine structure [129].

Self-organization driven by π–π interactions has meanwhile been exploited to assemble nanotubes from even more complex building blocks. To this end, Zhi et al. deposited tetrakis(tert-butyl)-naphthalocyaninato nickel complexes that form columnar structures on the pore walls of AAO hard templates by edge-on π–π stacking from a solution in THF [102]. After thermal annealing, a highly ordered columnar structure was obtained, and stable tetrakis(tert-butyl)-naphthalocyaninato nickel nanotubes could be released from AAO hard templates or converted into graphitic carbon nanotubes containing nitrogen or nickel nanoparticles. Liu et al. prepared nanotubes from sandwich-type (porphyrinato)(phthalocyaninato)europium(III) complexes [130].

However, the formation of mesophases inside the two-dimensional confinement of nanopores can be complex. For example, a model compound based on the triphenylene motif was melt-infiltrated into AAO hard templates. It was found that homeotropically anchored columns whose growth starts from the pore walls compete with planar columns in the center of the pores that proceed along the pore axes, i.e., along the direction that is free
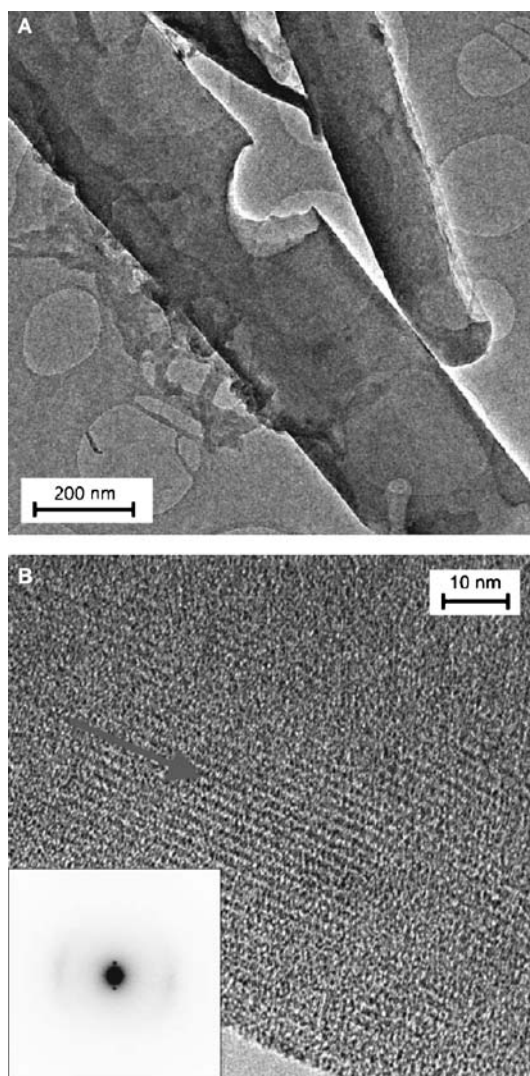
Fig. 16 TEM images of carbonaceous nanotubes obtained by assembling HBC molecules inside hard templates. **A** Defect evidencing their tubular structure. **B** Detail of the wall structure; the *arrow* indicates the directions of the columnar structures and the tube axis; *inset*: electron-diffraction pattern. Reproduced from [128]. © (2007) Wiley-VCH

of geometric constraints [65]. Whereas the planar phase was characterized by a narrow orientation distribution, the homeotropic phase was significantly less ordered. Pentacene nanotubes prepared by melt infiltration and slow cooling to room temperature [131] exhibited no long-range order. Also, HBCs that were designed in such a way that they anchor face-on on smooth sub-

strates did not yield nanotubes with uniformly oriented graphene layers when deposited into AAO templates [132]. Thus, it seems that the suppression of face-on anchoring leading to homeotropic orientation of the columns, for example by using molecular building blocks that tend to intercolumnar π–π stacking, results in the formation of highly ordered planar mesophases. However, homeotropic phases inside AAOs are characterized by a high degree of disorder. On the one hand, the curvature of the pore walls prevents a perfect parallel arrangement of the columns along the perimeter of the pores so that growing columns will impinge on their neighbors. On the other hand, the roughness of the pore walls may also introduce disorder.

5
Phase Separation in Nanoporous Hard Templates

5.1
Spinodal Decomposition in 2D Confinement

Phase separation processes have been widely used to generate mesostructured materials, such as controlled porous glasses [133]. It is obvious that the decomposition of mixtures in the pores of hard templates is a promising access to nanotubes with tailor-made fine structures. For example, nanotubes with walls exhibiting a microporous fine structure are potential components for storage devices or chromatographic separation processes. Nevertheless, this strategy is, up to now, largely unexplored, whereas a plethora of publications deal with decomposition processes in the course of electrospinning [134–136]. Phase boundaries may be crossed if a mixture is subjected to thermal quenching, or if the composition of the mixture changes because of the evaporation of a volatile solvent. Commonly, a spinodal decomposition [137, 138] sets in. Then, periodic composition fluctuations in an initially homogeneous system begin to grow. Simultaneously, ripening of the morphology starts, driven by the tendency to minimize the interfacial area between the coexisting phases, at the initial stage by conformational changes of the polymer chains and subsequently by Ostwald ripening [139]. For a broad composition range, the phase morphology generated by spinodal decomposition is initially a bicontinuous network of the two components that breaks up at later stages of the ripening process. The presence of interfaces modifies the decomposition process in that a surface-induced layered structure forms, a phenomenon known as "surface-directed spinodal decomposition" [140]. In thin films, the concentration waves emanating from the upper and lower surfaces may interfere [141]. If the film thickness is further reduced, a crossover from three- to two-dimensional spinodal decomposition kinetics occurs [142]. Therefore, it is to be expected that decomposition in a cylindrical or tubular geometry in contact with pore walls acting as

a rigid, non-critical matrix phase is modified as compared to bulk systems or thin film configurations. Predominantly liquid/liquid decomposition of binary mixtures in cylindrical pores has been studied theoretically [82, 83, 143–146]. As summarized by Gelb et al. [83] persistent metastable states occur within the two-phase region, resulting in common hysteretic behavior and a dependence of the phase morphology on the history of the sample, whereas macroscopic phase separation does not take place on experimentally accessible timescales. Moreover, critical temperatures and mole fractions are shifted.

If the pore walls are neutral with respect to the components of the mixture, a plug-like morphology develops with a domain size that saturates at a length scale far away from macroscopic phase separation [143, 144]. However, particularly the affinities of the components to the pore walls are important parameters governing decomposition processes in nanopores. Phase separation induced by thermal quenching might be accompanied by wetting transitions, that is, changes in the relative affinities of the components to the pore walls [84]. Dependent on the temperature, two equilibrium states were predicted. In the case of partial wetting, where both components are in contact with the pore walls, the equilibrium morphology consists of two cylindrical segments consisting of the pure components, which are separated by one interface stretching across the pore. However, long-lived metastable states characterized by a sequence of short plugs, each of which is in contact with the pore walls, were predicted to be more realistic. If the pore walls are completely wetted by one of the components, the non-wetting component forms a cylinder in the center of the pore surrounded by the wetting component that is exclusively in contact with the pore walls.

Apparently, no experimental studies of liquid/liquid decompositions of binary polymer mixtures confined to nanopores have been reported up to now. A possible reason for this lack of experimental work lies in the fact that the in situ monitoring of phase separation inside nanoporous hard templates is far from being trivial. As discussed above, the background scattering of the hard template is a severe drawback for SAXS. The information accessible by other methods such as DSC is limited. Moreover, given the importance of interfacial effects, it appears to be difficult to infiltrate molten polymer blends in such a way that the composition inside the pores corresponds to that of the bulk mixture on top of the hard template. It is reasonable to assume that the component with lower affinity to the pore walls will be expelled from the pores. The homogeneity of polymer blends on the mesoscopic length scales relevant to the infiltration of nanopores is certainly another issue to be considered. The most straightforward way to infiltrate mixtures containing at least one polymeric component into nanoporous hard templates is wetting with homogeneous solutions in a common volatile solvent. However, the presence of a third, evaporating component complicates the understanding of the involved structure formation processes. The analysis of the phase morphology obtained in this way was, up to now, limited to SEM and TEM in-

vestigations of nanotubes and nanorods in which the structure evolution was frozen.

As model systems, mixtures of PLA and organometallic complexes containing Pd and Pt dissolved in a common solvent were filled into the pores of hard templates [85, 147]. After the evaporation of the solvent, tubes with a wall thickness of a few tens of nm were formed in which the metal precursors were dispersed. After thermolytic reduction, the evolution of nanoparticles consisting of the elemental metals inside the liquid polymeric matrix
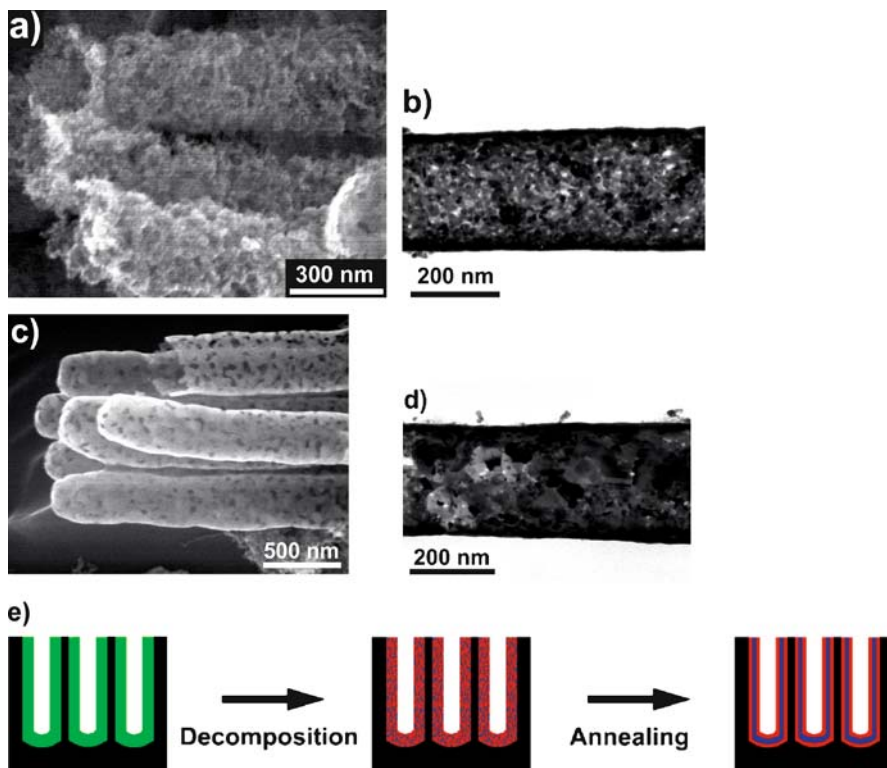

Fig. 17 Palladium nanotubes obtained by the ripening of Pd nanoparticles in a PLA matrix after spinodal decomposition of a PLA/palladium acetate/solvent mixture inside AAO and pyrolytic degradation of PLA. **a** SEM and **b** TEM image after short ripening times; **c** SEM and **d** TEM image after longer ripening times. **e** Schematic diagram of the ripening process. After the decomposition of the initially homogeneous mixture, the walls of the Pd nanotubes were at first rough, highly porous, and had obviously a reticular structure, which is indicative of an interpenetrating morphology with a small spinodal wavelength. At later ripening stages, the nanotube walls had a smoother, layer-like appearance, and the size of the Pd crystals significantly increased, which is indicative of the evolution of a coarser, layered structure and surface-induced ordering. Panels **a**–**d** are reproduced from [63]. © panels **a**–**d** (2004) Wiley-VCH

was monitored as a model process for spinodal decomposition and morphology ripening. The ripening was stopped by pyrolytic degradation of the PLA. After short ripening times, for example, the walls of Pd nanotubes were rough, highly porous, and had obviously a reticular morphology (Fig. 17a,b). At later ripening stages, the nanotube walls had a smoother, layer-like appearance, and the size of the Pd crystals significantly increased (Fig. 17c,d). Thus, after short ripening times, the initially homogeneous tube walls are characterized by an interpenetrating morphology with a small spinodal wavelength. Further ripening results in the evolution of a coarser, layered structure that is indicative of surface-induced ordering (Fig. 17e). Wetting AAO templates with solutions containing a polymeric wetting carrier and precursors for magnetic metals such as cobalt was applied to synthesize magnetic nanotubes [148, 149].

Surface-induced ordering was also observed in nanotubes obtained by deposition of a solution containing PMMA and a discotic liquid crystal of the triphenylene type into AAO templates with a D_p-value of 400 nm. The PMMA segregated to the pore walls, whereas the liquid crystal enriched at the inner surface of the nanotubes (Fig. 18a). It was assumed that the synergistic interplay of two different physico-chemical phenomena led to a surface-directed phase separation. First, low molecular mass species such as the triphenylene compound enrich at interfaces in the presence of a polymer for entropic reasons [150, 151]. Secondly, taking into account the high compatibility of the liquid crystal used and PS, PMMA should have a higher affinity to the AAO pore walls [152–154]. Reducing the D_p-value of the AAO hard template to 60 nm resulted in the occurrence of a striking morphological crossover. Solid nanorods were obtained with a disordered segmented morphology (Fig. 18b). The disappearance of the inner tube surface obviously resulted in a competition of the enthalpic and entropic effects: the PMMA tends to segregate to the pore walls for enthalpic, and the triphenylene compound for entropic rea-
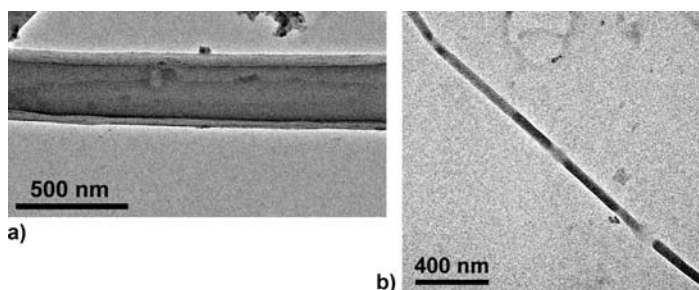

Fig. 18 PMMA/discotic composite nanofibers prepared inside AAO hard templates. **a** Nanotube (diameter about 400 nm) with a wall consisting of an outer PMMA layer and an inner (stained) discotic layer; **b** nanorod (diameter 60 nm) with a disordered segmented morphology. Reproduced from [65]. © (2005) Wiley-VCH

sons. Since only one interface at the pore walls instead of two interfaces in a tubular configuration was available, the formation of a layered structure was prevented. Thus, a confinement-induced transition from a wetting state (one phase of a critical two-phase system in exclusive contact with an interface) to a non-wetting state (both phases in contact with the interface) occurred.

5.2
Sol/Gel Chemistry with Block Copolymer Soft Templates

Spinodal decomposition is a straightforward access to mesostructured materials characterized by a certain degree of near order. However, phase separation can even be exploited to fabricate ordered mesostructured materials if amphiphilic species acting as soft templates are involved. Well-established syntheses for mesoporous materials with mesopore diameters ranging from a few nanometers up to a few tens of nanometers start with sol solutions containing either low molecular mass surfactants [155–157] or BCPs containing blocks with different polarity [158, 159] and precursors for scaffolds consisting of inorganic oxides or amorphous carbon [160–165]. The precursor for the scaffold material commonly segregates into the polar phase defined by the soft template that self-assembles if its concentration is larger than the critical micelle concentration. Subsequently, the morphology thus formed is fixated by a gelation or aging step in which the precursors for the inorganic scaffold materials are crosslinked. Subsequent high-temperature calcination yields inorganic scaffolds containing highly ordered mesopore arrays. Several excellent review articles summarize syntheses for mesoporous materials and their properties [166–172]. However, they are typically obtained in the form of powders consisting of randomly oriented grains. On solid substrates, the mesopores are arranged parallel to the substrate surfaces, a morphology that is of limited use for applications in the fields of separation, catalysis, and storage. Strategies to overcome this drawback based on surface modifications or the freezing of non-equilibrium structures only yield thin mesoporous layers with mesopores having limited aspect ratios. Therefore, it is still challenging to fabricate free-standing mesoporous membranes having the mesopores oriented normal to the plane of the membrane by approaches based on sol/gel chemistry. In order to address this problem, the self-assembly of BCP soft templates inside the pores of hard templates has emerged as a promising synthetic strategy, taking advantage of the availability of mechanically stable, extended membranes having larger but properly oriented membrane pores (Sect. 2).

   The first reported procedures for the preparation of mesoporous silica nanofibers by means of BCP soft templates inside hard templates were adaptations of synthetic strategies introduced by Stucky and coworkers [159]. Both tubular and solid entities with a mesoporous fine structure can thus be prepared. In their pioneering work, Yang et al. filled sols containing Pluronic

F127 and TEOS into AAO hard templates with a D_p-value of about 250 nm. Inside non-modified AAO the mesoporous silica remained attached to the oxidic, polar pore walls of the hard template so that tubes formed. However, if the hard templates were modified with hydrophobic silane coupling agents, the silica detached from the pore walls of the hard template, and solid rods were obtained [173]. Liang and Susha reported that infiltration of sols into polycarbonate membranes yielded tubular structures if the sols had high ethanol content, whereas solid rods formed when the ethanol content was reduced [174]. Both Liang and Susha, as well as Yao et al. [175] moreover found that aging the sols inside the pores of a hard template in the presence of an external bulk sol reservoir promotes the formation of solid mesoporous silica fibers, whereas the removal of excess sol from the surfaces of the hard templates after the infiltration promotes the formation of tubular structures. Zhu et al. obtained tubular structures in AAO templates with a D_p value of about 200 nm by slow infiltration of mixtures containing prehydrolized TEOS [176]. To this end, a sol solution was cast onto a smooth substrate. After placing AAO hard templates on top of the sol films, the samples were annealed at 100 °C. The lengths of the silica nanotubes thus obtained ranged from 500 nm for a heating time of 2 h up to 10 μm for longer heating times. Apparently, the prehydrolized sol could slowly enter the pores governed by the capillary wetting mechanism (Sect. 3.3) but the reduced mobility of the sol apparently prevented the filling of the empty space inside the pores formed upon evaporation of the solvent. Thus, it appears that the nature of the pore walls, the composition of the infiltrated sol, and the amount of sol solution that can access the pores are parameters determining whether tubular or solid mesoporous silica structures form inside hard templates.

Gaining control over the orientation of the mesopores inside hard templates has turned out to be a delicate challenge. Subtle changes of parameters such as the composition of the sol or aging conditions lead to striking changes of the mesopore structure, which is in turn affected by the two-dimensional geometric confinement imposed by the pore geometry and the nature of the pore walls. In the case of mesoporous materials, the bulk morphology of which is characterized by hexagonal arrays of aligned mesochannels, the mesopores formed by self-assembly of BCP soft templates inside the pores of hard templates may align with the long axes of the hard template pores, or they adopt the contour of the pore walls and wind about the long axes of the hard template pores. If the hard templates have pores smaller than about 100 nm, new and unprecedented morphologies are obtained that are substantially different from their bulk counterparts, as discussed below. Self-assembly of different BCP soft templates of the Pluronic type inside the pores of hard templates with D_p-values of a few 100 nm yielded hexagonal arrays of mesopores winding about the long axes of the mesoporous silica nanofibers [173, 174, 177] (Fig. 19), as well as hexagonal mesochannel ar-
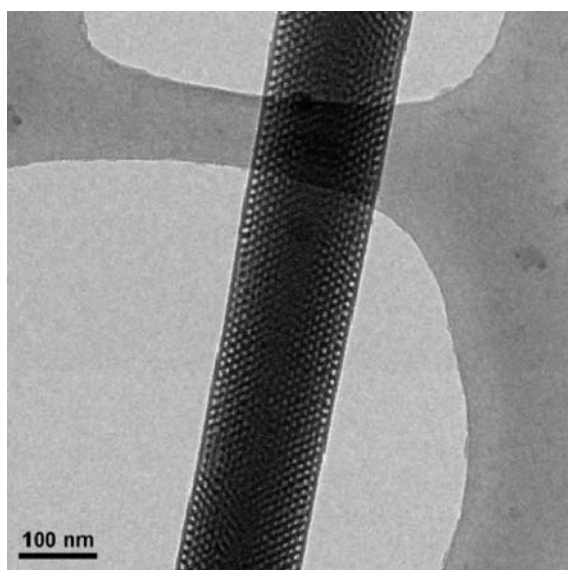
Fig. 19 Example of a mesoporous silica nanofiber containing hexagonal arrays of mesopores winding about the fiber axis. Reproduced from [177]. © (2005) American Chemical Society

rays [178] and concentric-lamellar structures [179] aligned with the fiber axes.

The relative orientation of hexagonal mesopores inside hard templates with a D_p-value of about 200 nm was studied by several authors and depends both on the composition of the sol and on the aging conditions. Yang et al. reported that an increase in the concentration of the BCP soft template in the sol solution led to a crossover from circular mesopores perpendicular to the long axes of the hard template pores to mesoporous channels aligned with the long axes of the hard template pores [173]. Platschek et al., who investigated the self-assembly of BCP and surfactant soft templates in AAO hard templates by means of TEM and grazing incidence SAXS, reported that a drastic shift in population from a circular pore arrangement towards a columnar arrangement of the mesopores aligned with the long axes of hard template pores (Fig. 20) occurred along with an increase in surfactant concentration in the sols or environmental humidity [180]. Under conditions characterized by high humidity and high surfactant concentration, the time required for evaporation of the solvent was extended so that a columnar morphology appearing to be closer to equilibrium could be attained. The presence of water during gelation was also highlighted as a key parameter determining the pore arrangement by other authors. Jin et al. observed mesopores partially aligned with the hard template pore axes in the center of the mesoporous entities surrounded by circular mesopores in samples aged in the absence of
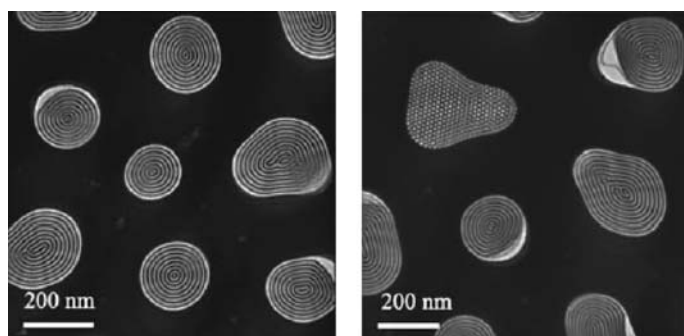
Fig. 20 Plan-view TEM images of mesoporous silica nanofibers with dominant circular orientation of the mesopores. Reproduced from [180]. © (2006) Wiley-VCH

water, whereas in samples aged in the presence of water a circular arrangement of the mesopores was found [181]. These authors assumed that the presence of water in the sol would retard the evaporation of the volatile solvents and concluded that the circular pore configuration would correspond to the equilibrium. Yao et al. reported that in as-prepared silica nanofibers the mesochannels are oriented parallel to the long axes of the hard template pores in the absence of water, or perpendicular in the presence of water during aging and related this observation to the acceleration of the hydrolysis of the silica precursor TEOS caused by the presence of water [175]. Hence, the configuration obtained in the absence of water, that is, hexagonal mesopore arrays parallel to the long axis of the hard template pores would correspond to the equilibrium. Despite these somewhat inconsistent findings and conclusions drawn by different authors, it seems to be unambiguous that the stage at which the assembly of the soft template is frozen determines the morphology of the mesoporous nanofibers. Apparently, the mesoscopic structure results from counteracting growth modes governed by surface-induced ordering and the two-dimensional confinement imposed by the geometry of the hard template pores. It is noteworthy that inside macroporous silicon with a pore diameter of $1\,\mu m$ no preferred mesopore orientation was found. Instead, the mesoporous microfibers consisted of segments with different mesopore orientations [19].

An interesting procedure for the incorporation of cadmium selenide nanoparticles into mesoporous silica nanofibers involves the use of sols containing Cd(II) species [177]. After the gelation step and prior to calcination, the Cd was converted into CdS by exposing the samples to gaseous H_2S. Whereas in the case of a small Cd(II) content in the sol solutions hexagonally ordered circular mesopores winding about the long axes of the hard template pores were obtained, higher Cd(II) contents led to the generation of disordered pore structures along with a significant increase in the specific surface, as determined from adsorption isotherms. Also, the average size

of the CdSe nanoparticles could be increased by increasing the Cd(II) content in the sol, as evidenced by absorption spectroscopy and the shift of the band-edge emission in the PL spectra.

Whereas in the works reviewed above predominantly AAO hard templates with a D_p-value about one order of magnitude larger than the periods of the BCP soft templates were used, Wu et al. systematically studied the self-assembly of $EO_{20}PO_{70}EO_{20}$ inside AAO hard templates having D_p-values from 80 down to 20 nm [182, 183]. Inside such narrow pores, bulk-like morphologies were completely suppressed. For D_p-values between 55 and 73 nm,
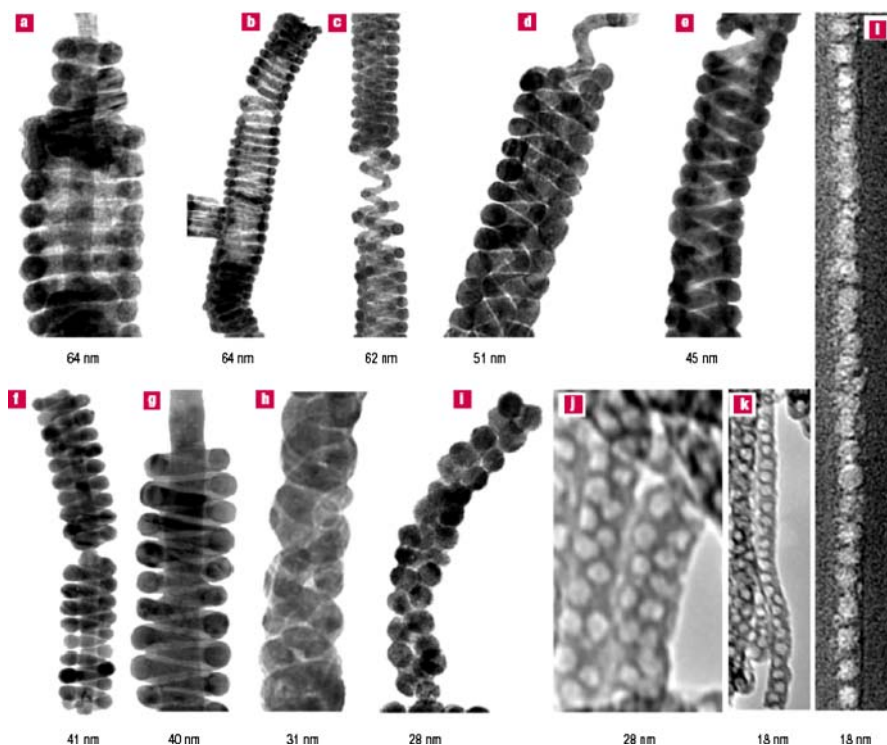

Fig. 21 TEM images of mesostructures formed inside AAO with differing confinement dimensions. The confining nanochannel diameter is indicated underneath each image. **a–i** Silver inverted mesostructures prepared by backfilling the confined mesoporous silica; **j–k** free-standing mesoporous silica fibers; **l** mesoporous silica embedded inside the AAO obtained using a focused ion beam for sample preparation. The structures are **a** three-layer stacked doughnuts; **b** S-helix; **c** core–shell D-helix, in which the core and the shell are both S-helix; **d** core–shell triple-helix, in which the shell is a D-helix and the core is a S-helix; **e** D-helix; **f,g** S-helix with a straight core channel; **h** D-helix; **i,j** inverted peapod structure with two lines of spherical cages packed along the long axis of the alumina nanochannel; **k,l** inverted peapod with one line of cages. Reproduced from [182]. © (2004) Nature Publishing Group
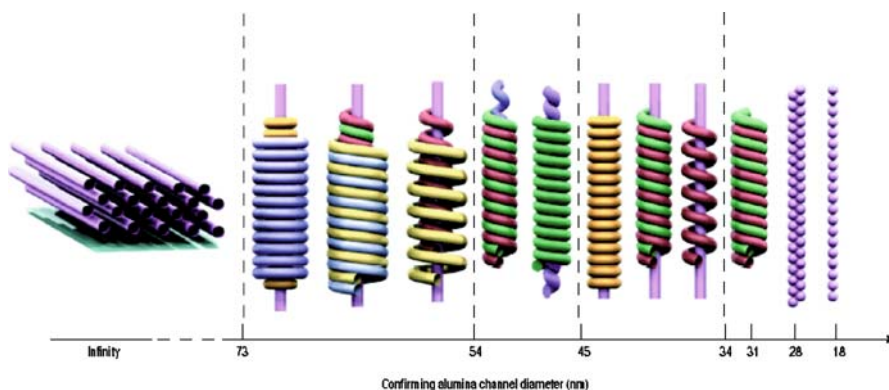
Fig. 22 Summary of the experimentally (cf. Fig. 21) observed confined mesostructural evolution with varying D_p-value. Reproduced from [182]. © (2004) Nature Publishing Group

the mesostructures were composed of a straight core and two more coaxial layers consisting of concentric mesochannels with morphologies as diverse as stacked doughnuts, single helices or double helices (Figs. 21, 22). For D_p-values ranging from 49 to 54 nm, coaxial double layer helices were found, for D_p-values ranging from 34 to 45 nm a straight inner core was surrounded by one coaxial layer of the helical or stacked doughnut type, for a D_p-value of 31 nm a single helix was observed, and for smaller D_p-values spherical mesopores arranged in one or two rows formed (Figs. 21, 22). Analogous to the conceptualization of the structures of carbon nanotubes, Wu et al. suggested a rolling scheme to derive the morphologies obtained in the two-dimensional confinement of the hard template pores from thin-film morphologies. A progression of mesoscopic structures in two-dimensional confinement well in line with the experimental results was obtained by means of self-consistent field calculations with a liquid diblock copolymer/homopolymer mixture as a model system. Moreover, it is remarkable that chiral structures such as helices were obtained from achiral materials, even though a chiral induction leading to enantiomeric excess has not been reported up to now.

One of the few reports on the preparation of mesoporous silica nanofibers with a soft template other than triblock copolymers of the Pluronic type deals with the synthesis of silica nanofibers with high aspect ratios containing linear arrays of mesopores by a solution-induced self-assembly process (Fig. 23), as previously reported for thin-film configurations [184]. To this end, PS-*b*-PEO diblock copolymers were employed as structure-directing agents in sol solutions containing toluene/ethanol mixtures. For a D_p-value of 35 nm, a single line of mesopores formed, for a D_p-value of 60 nm two parallel rows of mesopores were obtained [185].

Fig. 23 TEM image of released silica nanowires containing a single row of mesocages obtained with PS(9500)-*b*-PEO(9500) as the soft template and an AAO hard template (D_p = 35 nm). Reproduced from [185]. © (2007) Wiley-VCH

Few efforts have been directed towards the fabrication of mesoporous nanofibers consisting of other inorganic oxides. Mesoporous titania nanofibers containing anastase crystallites with diameters of the order of 6.5 nm were obtained by Chae et al. by infiltration of sols containing $EO_{106}PO_{70}EO_{106}$ as a soft templat and titanium(IV)isopropoxide as a titania source [186] into AAO hard templates with a D_p-value of 200 nm. However, the mesopore arrays did not show long-range order. In a modified procedure with a low-viscous sol solution, Wang et al. fabricated nanotubes the walls of which consisted of mesoporous titania exhibiting hexagonal mesopore ordering [187]. The evolution of a tubular structure was attributed to the high affinity of the gel to the alumina pore walls, resulting in volume shrinkage towards the pore walls of the hard template.

As compared to mesoporous oxide nanofibers, much lesser attention has been paid to their mesoporous amorphous carbon analogues. However, mesoporous carbon exhibits superior resistance to acids and bases, excellent heat resistance, as well as high intrinsic electric conductivity. Potential applications for hybrid membranes consisting of mesoporous carbon within hard templates include size-selective electrosorption, electrosynthesis of nanostructures, catalysis, separation and storage. The first reported procedure for the synthesis of mesoporous carbon nanofibers involved the preparation of

a sacrificial Fe-containing mesoporous silica scaffold inside an AAO hard template with a D_p-value of about 200 nm, exposure to hydrogen at 750 °C, incorporation of carbon by supercritical fluid deposition of a xylene/CO_2 mixture, and removal of both the AAO hard template and the sacrificial silica scaffold by etching with hydrofluoric acid [188]. While the mesoscopic fine structure of the mesoporous carbon nanofibers was a perfect replica of the silica scaffold, the AAO hard template is inevitably destroyed upon removal of the silica scaffold. Consequently, hybrid membranes containing mesoporous carbon inside an AAO matrix are not accessible by this approach. This drawback can be overcome by directly synthesizing mesoporous amorphous carbon inside the pores of the hard template. Zheng et al. infiltrated a mixture of Pluronic F127 ($EO_{106}PO_{70}EO_{106}$) as a structure directing soft template and resol as a carbon precursor dissolved in ethanol into AAO hard templates. After the evaporation of the ethanol, gelation and carbonization at 700 °C in nitrogen, mesoporous carbon nanowires were obtained. Inside AAO hard templates with a D_p-value of about 300 nm a core/shell structure was obtained in which a stack of layers perpendicular to the nanowire axis surrounded a core containing pores winding about the nanowire axis. At the same time, an approach based on solvent-free infiltration was reported. A solution of Pluronic F127, phloroglucinol as a carbon source, formaldehyde and traces of HCl in an ethanol/water mixture was stirred at room temperature until a separation into an upper water/ethanol phase and a lower polymerrich phase occurred. The supernatant solvent-rich phase was removed, and the lower polymer-rich phase was spread on AAO hard templates. Gelation of the infiltrated mixture and subsequent calcination at 500 °C yielded mesoporous amorphous nanofibers with a core characterized by a bicontinuous morphology, as desired for applications in the field of separation, catalysis and storage [189]. Again, a layered shell indicative of surface-induced ordering was found that was in turn surrounded by a continuous outermost carbon wall. Whereas the removal of volatile solvents prior to the infiltration may be a measure to minimize volume shrinkage, the low carbonization temperature is important for the fabrication of mesoporous amorphous carbon/AAO hybrid membranes, because the carbonization can be performed while the AAO membrane is still attached to an underlying Al substrate. This configuration is advantageous because the Al substrate stabilizes the AAO layers so that residual material can easily be removed from their surfaces to uncover the pore openings. Selective etching steps can then be applied to remove the Al and to open the pore bottoms. Optionally, an Al ring surrounding the area in which the pore bottoms are open can be conserved to mechanically stabilize the membrane. It is interesting to note that the fiber core vanishes when the D_p-value of the hard template is decreased below 100 nm. Arrays of freestanding mesoporous amorphous carbon nanofibers on silicon substrates using Pluronic F-127 as a structure-directing soft template were prepared by Wang et al. by placing an AAO hard template on the

substrate [190]. After gelation and calcination, a supercritical drying process was applied to avoid condensation of the aligned mesoporous amorphous carbon fibers after the wet-chemical etching of the hard template. Their internal mesopore morphology resembled that previously found for mesoporous silica nanofibers and consisted of circular mesopores perpendicular to the long axes of the nanofibers that occasionally surrounded a core of mesopores aligned with the long axis of the nanofibers.

It is obvious that hybrid systems of AAO hard templates containing mesoporous nanofibers obtained by self-assembling BCP soft templates are of considerable interest for a plethora of applications in the fields of catalysis, separation and storage. However, the combination of sol/gel chemistry and high-temperature calcination steps is accompanied by pronounced volume shrinkage of the mesoporous material. Solvent evaporation during the initial gelation step performed at room temperature results in unidirectional shrinkage of up to 20% [191], and further cross-linking as well as calcination lead to unidirectional shrinkage of about 15–40%, depending on the protocol applied [192]. Yao et al. noted that shrinkage inside AAO hard templates occurs primarily in a direction perpendicular to the AAO pores with void space being created at the silica–alumina interface [175]. Given the high affinity of the sol-gel to the pore wall, it is reasonable to assume that large-scale shrinkage in the vertical direction is prevented rather than shrinkage in the transversal direction. Consequently, the length of the hard template pore segments filled with the mesoporous material can hardly be controlled in a rational manner. Moreover, the mesoporous material occupies only a certain portion of the cross-sectional area of the hard template pores so that large voids and empty spaces occur. It is obvious that these structural defects will deteriorate the performance of the hybrid membranes.

Yamaguchi et al., who prepared microporous silica inside AAO hard templates with a D_p-value of 200 nm using cetyltrimethylammoniumbromide as a low molecular mass soft template, demonstrated size-selective separation of a set of model compounds [193]. However, to this end, a non-calcinated AAO membrane containing a silica-surfactant nanocomposite was used. Replacing calcination by extraction is another approach to overcome undesired volume shrinkage of mesoporous nanofibers inside hard templates. Yoo et al. prepared at least partially cubic mesoporous silica inside AAO with a D_p-value of about 200 nm using Brij-56 as a surfactant and removed the latter by extraction with ethanol [194]. Four successive infiltration/drying/surfactant extraction cycles yielded AAO/mesoporous silica hybrid membranes that exhibited excellent helium/nitrogen permselectivity with permselectivity values at the theoretical Knudsen limit. This result indicated the absence of "pinhole defects". Therefore, a defect-free, uniform filling of the AAO pores with mesoporous silica could be evidenced. Another interesting application reported for released mesoporous titania nanotubes, thus insensitive to volume shrinkage, is their use as nanostructured electrode material having outstandingly

high specific surface area [187]. Electrons injected into the titania scaffold can rapidly be transferred into electrolyte solutions. The mesoporous titania nanotubes were characterized by large specific capacity and a high charge-discharge rate. Even though a small number of applications for either released mesoporous nanofibers or hybrid membranes containing mesoporous nanofibers synthesized by means of sol-gel chemistry with BCP soft templates have been reported, it appears that these materials still need to be optimized for real-life applications.

5.3
Microphase-Separated Block Copolymer Melts

Liquid block copolymers consisting of immiscible blocks are known to self-assemble into ordered periodic arrays of nanoscopic domains [195–197]. Hence, infiltration of BCP melts in hard templates is an alternative to sol/gel chemistry that yields complex polymeric nanofibers with an adjustable fine structure. As discussed in Sect. 3.3, capillary wetting governs the filling of nanopores with BCP melts. Threads of liquid but microphase-separated BCPs preceded by menisci slowly move into the pores of the hard templates. The time scale on which this process takes place allows controlling the length of the BCP nanofibers by quenching the BCP to a temperature at which it is solid. It is to be expected that the two-dimensional geometric confinement and the influence of the pore walls modify the microphase structure of the BCPs, as is the case in thin-film configurations, in which a one-dimensional confinement is imposed. Structure formation processes in thin BCP films have been studied intensively [198, 199]. A scenario in which BCPs self-assemble between smooth, non-competing surfaces exhibits, to a certain extent, similarities to the self-ordering of BCPs in nanopores. Whereas a large number of experimental publications deal with sol-gel chemistry inside nanoporous hard templates, no simulations of the related structure formation processes have been performed so far since the system appears to be too complex. In contrast to the lack of theoretical studies of the mesophase formation in confined multicomponent sol systems, the self assembly of BCP melts under cylindrical confinement was simulated in a considerable number of works.

In the case of diblock copolymer melts, which are the simplest model system for the elucidation of structure formation processes involving BCPs in nanoporous hard templates, only the two immiscible blocks have to be considered as components. Self-consistent field methods were applied to study the morphologies of liquid diblock copolymer/homopolymer mixtures that were considered as a model system for triblock copolymers in sol solutions [182], of pure diblock copolymer melts [200–202], and of order–disorder transitions in diblock copolymer melts [203]. For example, Li et al. found for a model diblock copolymer that forms cylinders in the bulk

a variety of novel microdomain structures. With increasing D_p-value a sequence of morphologies containing single cylinders, stacked disks, single helices, double helices, toroid-spheres, and helices-cylinders occurred [201]. Other studies dealing with the morphologies of diblock copolymers employed dynamic density functional theory [204] and dissipative particles dynamics [205, 206]. However, in most works Monte Carlo simulations were used to investigate the mesoscopic structures of BCP-containing systems. Systems that were studied include melts of symmetric [207–212] and asymmetric diblock copolymers [211–213], of triblock copolymers [214, 215], and even mixtures of diblock copolymers [216]. Taking into account that the pores in hard templates often exhibit deviations from an ideal circular cross-section, the results of Monte Carlo simulations in which channel-like confining geometries with non-circular cross-sections were assumed are of considerable interest [217].

It is beyond the scope of this review to discuss the results of the simulations available so far in detail. Instead, some general tendencies are highlighted. Four parameters that mainly govern the morphology formation of a BCP-containing system in a nanopore have been identified.

(i)   The type of equilibrium morphology into which a bulk BCP with given segment-segment interactions between its constituents and a given degree of polymerization self-assembles, depends on the volume fractions of its constituents. Under cylindrical confinement, the composition plays an important role too but does not exclusively determine which kind of equilibrium structure the BCP adopts.

(ii)   It is straightforward to combine the parameters that determine the degree of geometric confinement imposed on the system, that is, the overall degree of polymerization of the BCP and the D_p-value of the cylindrical pore. Often, a reduced pore diameter is introduced. This quantity was, for example, defined as D_p/L_0, where L_0 is the bulk period of the model BCP [213]. Erukhimovich and Johner, who attempted to put confined structure formation of BCPs into a more general context, suggested a dimensionless parameter that is the product of D_p and the wave number of fluctuations of a critical order parameter that determines the ordering in the corresponding bulk system [218]. Whereas the critical order parameter in the case of an order–disorder transition in a BCP melt is related to the concentration of the repeat units of its constituents, the more general definition of a reduced pore diameter allows the treatment of ordering in cylindrically confined systems to be extended to a broader range of structure formation processes.

(iii)   The degree of repulsion between the blocks of the BCP has turned out to be a crucial parameter for the structure formation under cylindrical confinement, being of considerably greater importance than for structure formation in bulk systems. For example, Feng and Ruckenstein

found structural transitions when the interaction parameter between segments of the two blocks was changed [211].

(iv) The "surface field" that describes surface-induced ordering is of similar importance for the structure formation of BCPs under cylindrical confinement as for corresponding thin-film configurations. Taking into account the well-known strong influence of surfaces on spinodal phase-separation processes in cylindrical pores (Sect. 5.1), it is not surprising that the affinity of the components of the BCP to the pore walls can even govern the evolution of the mesoscopic morphology. The transition from a non-neutral pore wall exclusively wetted by one of the components to a neutral pore wall that is in contact with both components can be accompanied by a fundamental morphology transition in the whole system. For example, Chen et al. reported for a symmetric diblock copolymer a transition from "stacked disk" morphology to "cylindrical barrel" morphology. In the former case, a weak surface field prevented preferential wetting, and both components were in contact with the pore walls. In the latter case, a strong surface field led to preferential wetting of the pore walls by one of the components. For weak and intermediate strengths of the surface field also helical and even catenoid-cylindrical structures occurred [210].

A plethora of new morphology types, some of which are characterized by very complex domain structures, were predicted (Fig. 24). In most publications, some tens of different morphologies identified by simulations were displayed as snapshots but not related to a quantitative order parameter [200–202, 213]. Simple morphologies found for symmetric diblock copolymers include the stacked-disc structure with lamellae oriented perpendicular to the long axes of the hard template pores, which occurs for weak surface fields, and a concentric cylinder structure with circular lamellae oriented parallel to the long axes of the hard template pores in the case of strong surface fields. Lamellar structures of the minority component in asymmetric block copolymers can be induced by the surface field emanating from the pore walls [201], and the occurrence of helical structure motifs was predicted for a broad range of diblock copolymer compositions, predominantly in the presence of weak surface fields. It should also be noted that the mesopore structures of the silica nanofibers obtained by Wu et al. by self-assembling a $EO_{20}PO_{70}EO_{20}$ triblock copolymer in a sol solution infiltrated in AAO membranes [182] fit into the overall picture. It is again remarkable that confinement-induced chiral structures are generated in systems containing only achiral components. As pointed out by Erukhimovich and Johner [218], the free energies of both enantiomeric morphologies are identical so that statistically equally frequent formation of right-handed and left-handed helices is to be expected.

The phase behavior of asymmetric diblock copolymers seems to be more complex than that of symmetric diblock copolymers and the phase behav-
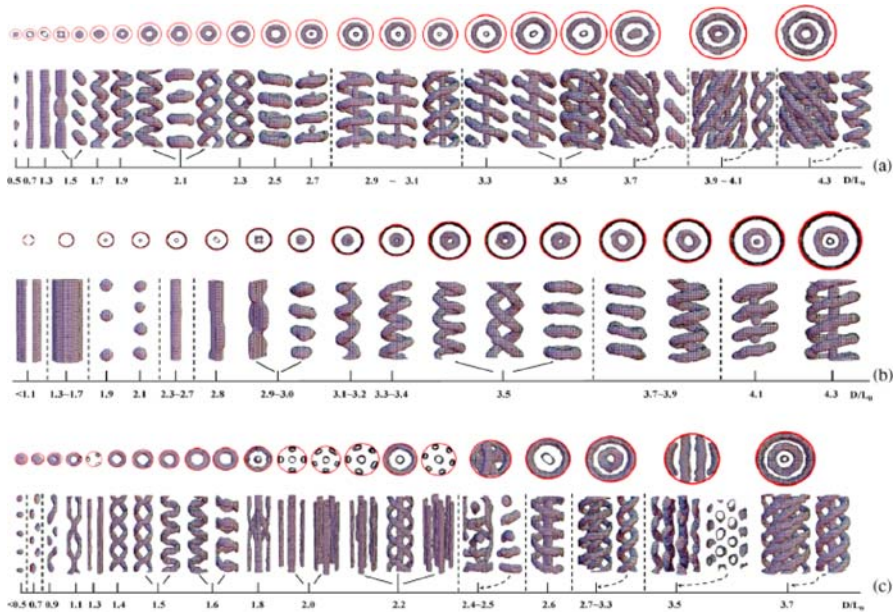
Fig. 24 Self-assembled morphologies of an asymmetric diblock copolymer confined to cylindrical pores obtained by a simulated annealing method as a function of the ratio D_p/L_0, where L_0 is the period of the BCP, for different wall-polymer interactions. The parameter D_p/L_0 is given underneath each morphology. The outmost circles in the top views indicate the wall of the cylindrical pores. For some large diameters, the inner ring is shown separately. **a** The pore wall attracts the majority blocks; **b** the pore wall attracts the minority blocks; **c** neutral pore walls. Reproduced from [213]. © (2006) American Physical Society

ior of triblock copolymers is more complex than that of diblock copolymers. In principle, it should be possible to determine phase diagrams displaying the dependence of the morphology type into which BCPs self-assemble under cylindrical confinement on each of the four parameters mentioned above, i.e., the relative volume fractions of the blocks, the reduced pore diameter, the segmental interaction parameters of the components and the surface field. However, apart from visualizing morphology snapshots, only a few attempts have been made to develop classical phase diagrams based on the relation of the body of identified morphologies to a quantitative order parameter. Erukhimovich and Johner derived reduced phase diagrams in which, for example, phase boundaries were displayed in the reduced temperature-reduced D_p plane for different surface field strengths [218]. Here, the reduced D_p-value is, as mentioned above, the product of D_p and the wave number of fluctuations of a critical order parameter determining the ordering in the corresponding bulk system, and the reduced temperature is related to the bulk order–disorder transition. Li et al. presented a phase
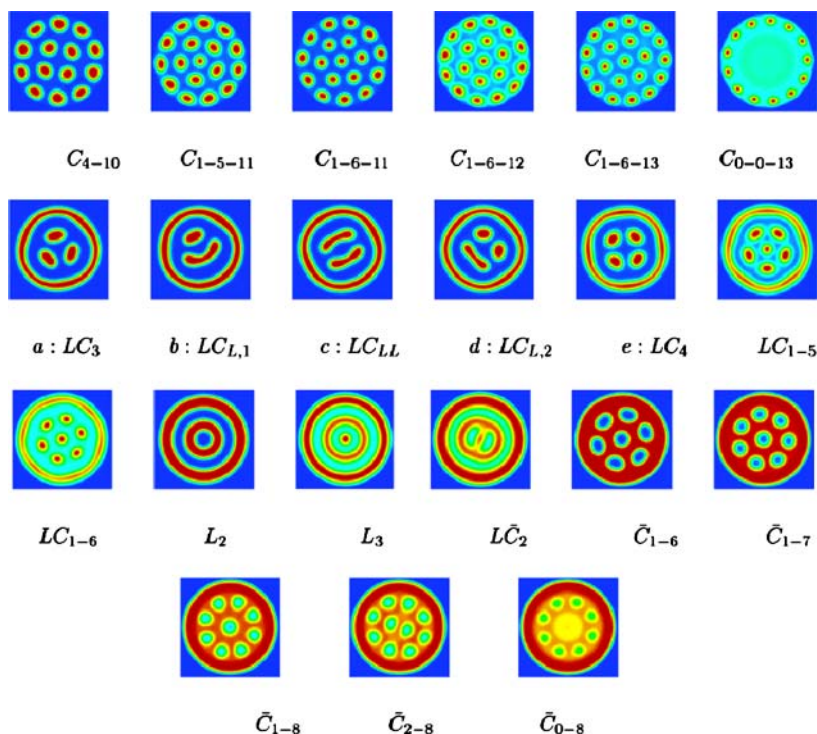
Fig. 25 Monomer density plots of the 21 nanostructured phases formed in a cylindrical pore with a D_p-value of 17 times the radius of gyration. The color ranges from *deep red* (A-rich regions) to *deep blue* (B-rich regions). The region outside the cylindrical pore is also colored deep blue. The notation C is used for cylindrical phases, L for lamellar phases, and LC for structures containing both lamellae and cylinders (intermediate structure). When the cylinders are composed of minority B component, an overbar is used. The number of cylinders in each ring, out from the center of the pore, is indicated by subscripts C_{i-j-k}. The number of L subscripts in the notation $LC_{L...L,i-j}$ indicates the number of lamellar segments in the inner region of a given intermediate structure. The second subscript indicates the number of cylinders of the minority species in the pore and whether these cylinders are arranged in rings. The stability regions for these structures are labeled on the phase diagram in Fig. 26. The notation (a, b, c, d, e) is used to label some of the intermediate phases in Fig. 26. Reproduced from [202]. © (2006) American Chemical Society

diagram for a diblock copolymer melt confined to a cylindrical pore with a D_p-value set to 17 times the radius of gyration of the model BCP in the $f - \chi N$ plane, where f is the volume fraction of one of the components, N the degree of polymerization of the BCP and χ the Flory–Huggins interaction parameter for the components of the BCP [202]. Figure 25 shows snapshots of the morphology types, and Fig. 26 the areas they occupy in the $f - \chi N$ plane. As compared to bulk systems and even thin film configura-
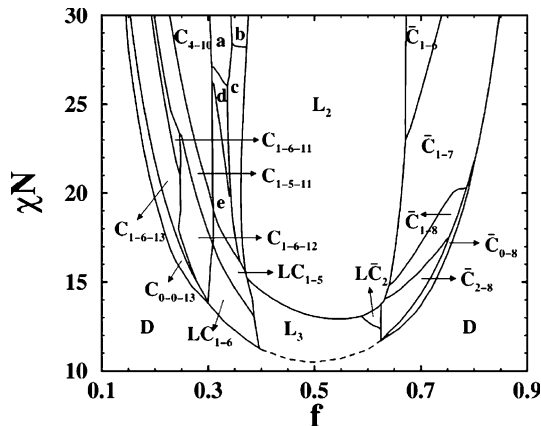
Fig. 26 Phase diagram for a diblock copolymer melt confined in a cylindrical pore with a D_p-value of 17 times the radius of gyration. The degree of polymerization of the copolymer is N, the Flory–Huggins parameter is χ, and f is the A monomer fraction. The disordered phase is labeled D; the other labels are as in Fig. 25. The *dashed curve* is an interpolation of the order–disorder transition curve. Reproduced from [202]. © (2006) American Chemical Society

tions, the phase behavior of BCPs under cylindrical confinement is much more complex.

Whereas the number of experimental publications dealing with sol-gel chemistry inside porous hard templates using BCP soft templates and that of theoretical papers dealing with self-assembly of BCP melts under cylindrical confinement is already large and increasing further, only a limited number of experimental reports on the self-assembly of BCP melts under cylindrical confinement are available up to now. However, BCP melts are an ideal system to explore the accessible morphology space since no fixation of non-equilibrium structures by gelation occurs, as in the case of sol-gel methods, and equilibrium structures can be obtained by thermal annealing or solvent annealing. Topographically patterned substrates have been used to increase the degree of order in thin BCP films confined to grooves or mesas [219–221]. However, up to now, only very few experimental studies of the structure evolution of BCPs under a true cylindrical confinement have been published. Russell and coworkers investigated PS-*b*-PBD diblock copolymers as a model system with highly repulsive blocks [74, 222]. In the case of symmetric PS-*b*-PBD that forms lamella in the bulk, concentric lamellae along the axes of the hard template pores were found. The PBD preferentially segregated to the pore walls, and alternating PS and PBD layers occurred and were visualized by TEM on ultrathin sections of the nanofibers in which the PBD was selectively stained (Fig. 27A). For ratios D_p/L_0 larger than 3.2 an outermost PDB layer was generally observed. A decrease in D_p led to a smaller number of concentric layers, whereas in the center either PS or PBD was located, de-
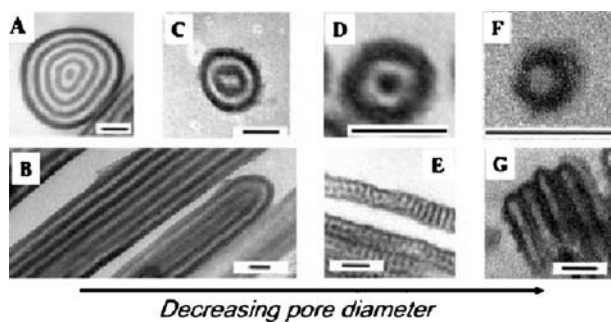
Fig. 27 TEM cross-sectional images of bulk lamella-forming PS-*b*-PBD confined in cylindrical pores. **A,C,D,F** Views across pore; **B,E,G** Views along pore; **A,B** $D_p/L_0 > 3.2$; **C** $D_p/L_0 = 3.2$; **D,E** $D_p/L_0 = 2.6$; and **F,G** $D_p/L_0 > 1.9$. *Scale bars*, 50 nm. Reproduced from [222]. © (2005) Wiley-VCH

pending on D_p (Fig. 27B,C). A deviation of the apparent repeat period from L_0 was found that increased for a given D_p-value towards the center of the pores where the layers exhibited the largest curvature, and for decreasing D_p-values. If D_p is comparable or even smaller than L_0 and D_p/L_0 is not an integer, the period of the BCP and the pore diameter are incommensurate. For $D_p/L_0 \approx 2.6$ a transition from a lamellar to a stacked disc or torus-type structure occurred. Normal to the rod axis, concentric layers were observed with PBD located at the centers and walls of the nanofibers. Along the axes of the nanorods, a stacked PS lamellar structure with a central spine and outer edges of PBD occurred (Fig. 27D,E) [223]. This morphology type has no counterparts in bulk systems but is in line with some of the theoretical predictions reviewed above. Further decreasing D_p/L_0 to a value of ≈ 1.9 resulted in another morphology transition. The pores of the hard template accommodated only one period, and the nanofibers consisted of a central core of PS, surrounded by a layer of PBD (Fig. 27F,G). This morphology requires a significant deformation of the BCP chains. However, concentric layers along the pores were apparently stabilized by the strong immiscibility of PS and PBD and favorable interfacial interactions of PBD with the pore walls [223].

In the case of asymmetric PS-*b*-PBD forming cylinders in the bulk, circular PBD layers parallel to the long axes of the hard template pores surround an area in which hexagonally packed PBD cylinders oriented along the pore axes are embedded in a PS matrix (Fig. 28A,B). However, the shape and size of the pores place constraints on the packing and both symmetry and separation distance of the domains were altered [74]. A decrease in D_p resulted in fewer cylinders within the cross-sectional area of the BCP nanofibers (Fig. 28C). Further decrease in D_p to values of 56–66 nm ($D_p/L_0 \approx 1.9$–2.3) led to the formation of a single cylindrical PBD domain in the center of the nanofibers with a PBD rim contacting the pore wall (Fig. 28D). The interfaces between the PBD center and rim and the PS showed undulations arising from the severe
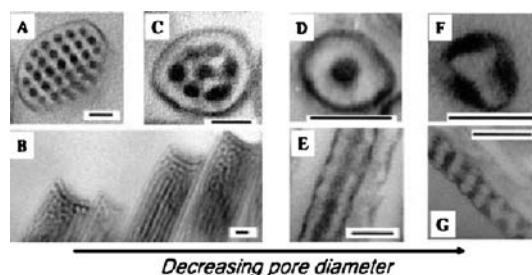
Fig. 28 TEM cross-sectional images of bulk cylinder-forming PS-*b*-PBD confined in cylindrical pores. **A, C, D, F** Views across pore; **B, E, G** views along pore; **A, B** $D_p/L_0 > 4$; **C** $D_p/L_0 = 4$; **D, E** $D_p/L_0 = 1.9–2.3$; and **F, G** $D_p/L_0 = 1.1–1.5$. *Scale bars*, 50 nm. Reproduced from [222]. © (2005) Wiley-VCH

geometric confinement, which were interpreted as a precursor to a change in the morphology (Fig. 28E) [222]. For D_p-values in the range from 33 to 45 nm ($D_p/L_0 \approx 1.1–1.5$), the PBD domain was still located at the pore walls, highlighting the edges of the nanofibers. However, instead of cylindrical domains aligned along the hard template pore axis, helical PBD structures maintaining contact with the pore walls were found whose pitch of 30 nm was close to L_0 (Fig. 28F,G) [224].

In another study, the diameter dependence of the morphology of symmetric PS-*b*-PMMA forming lamellae in the bulk ($L_0 = 42$ nm) on D_p was investigated [75]. In contrast to PS-*b*-PBD, PS-*b*-PMMA is only weakly segregated. However, the morphologies identified were similar to those obtained in the case of symmetric PS-*b*-PBD. Using AAO hard templates with D_p-values of 400, 180, 60 and 25 nm, a successive decrease in the number of concentric layers oriented parallel to the long axes of the hard template pores was found. For a D_p-value of 60 nm, a single circular PS layer surrounded a PMMA cylinder in the center of the nanofibers, and for a D_p-value of 25 nm, apparently a PS core was surrounded by a PMMA shell.

The morphologies of diblock copolymers under cylindrical confinement reported in experimental works are in line with the theoretical predictions reviewed above. However, because of the small number of publications addressing this issue, only a limited range of the anticipated morphology space has been explored. For example, no systematic variation of the surface field has been realized by modifying the pore walls of the hard template in such a way that their character changes form non-neutral to neutral. The limited interest in the investigation of the self-assembly of BCP melts inside hard templates might be due to the fact that, in contrast to the fabrication of mesoporous nanofibers by means of sol-gel chemistry, no obvious application exists. However, BCP nanofibers with complex morphologies consist of chemically distinct blocks. Therefore, it should be possible to realize selective segregation of precursors into one of the domains, a strategy that has suc-

cessfully been applied in the case of thin film configurations. Therefore, BCP nanofibers having a complex morphology should have great potential as a soft template system in the synthesis of advanced functional one-dimensional nanostructures.

6
Multilayer Nanotubes by Layer-by-Layer Deposition

In the previous sections, approaches to the generation of mesoscopic fine structures in tubular but also solid one-dimensional nanostructures were discussed that involved deposition of target materials or precursors thereof into porous hard templates by a single infiltration step. Subsequently, the supramolecular organization is guided by the geometric confinement and interfacial interactions with the pore walls. Layer-by-layer deposition [225–227] is a generic access to nanoscopic multilayer systems with controlled composition that differs from single-step infiltration methods in that a series of successive deposition steps is performed, the number of which determines the properties of the nanotubes thus obtained to a large extent. To attach a new layer to the layers already deposited, specific interactions between the involved species or molecular recognition mechanisms are exploited. Initially, the layer-by-layer technique was applied to consecutively deposit oppositely charged polymeric polyelectrolytes from diluted solutions. Whereas the electrostatic repulsion between equally charged species limits the thickness of a deposited layer, the electrostatic attraction between the alternating oppositely charged layers is the glue holding together the entire assembly. The number of deposition steps determines the number of bilayers formed and therefore the thickness of the entire multilayer. Moreover, it is possible to incorporate inorganic nanoparticles if their surfaces are charged [228, 229]. Therefore, layer-by-layer assembly allows fabricating nanoscopic functional multilayer systems with outstandingly high precision. Whereas at first smooth substrates had been functionalized in this way, the coating of colloidal polymer particles with a multilayer structure consisting of silica nanoparticles and polymeric polyelectrolytes was reported by Caruso et al. in 1998 [230]. It was further shown that hollow capsules with walls consisting of polymeric multilayers can be prepared if polymeric colloidal particles are used as sacrificial templates [231]. Calcination of colloidal polymer particles covered by a multilayer structure in which silica nanoparticles were incorporated led to the formation of hollow silica capsules [232]. Several excellent reviews deal with the fabrication of free-standing and three-dimensional nanostructures by layer-by-layer deposition [233–235].

It appears to be straightforward to fabricate polymeric tubular structures with complex but well-controlled wall morphologies and adjustable wall thickness by performing layer-by-layer deposition into porous hard tem-

plates. To this end, Ai et al. employed a pressure-filter-template technique to deposit poly(allylamine hydrochloride as the anionic and poly(styrene-sulfonic acid) as the cationic component from aqueous solutions also containing NaCl into AAO with a D_p-value of about 200 nm. After starting the deposition sequence with the formation of a poly(allylamine hydrochloride) layer directly on the pore walls, stable but flexible nanotubes consisting of three bilayers with a wall thickness of 50–80 nm were obtained even after etching the hard template with aqueous NaOH solution [236]. The thickness of the nanotube walls was one order of magnitude larger than that of corresponding multilayer structures prepared on smooth substrates in which a bilayer has a thickness of a few nanometers. Using PC membranes with a D_p-value of 400 nm and a T_p-value of 10 μm whose walls were initially coated with poly(ethylenimine), poly(acrylic acid)/poly(allylamine hydrochloride) multilayers were deposited onto the pore walls in the presence of Cu^{2+} and then thermally cross-linked. Moreover, positively charged Au nanoparticles were incorporated in nanotube walls in alternation with four-layer polyelectrolyte structures, and negatively charged semiconductor nanoparticles in alternation with three-layer polyelectrolyte structures. Whereas the wall thickness of the nanotubes thus obtained, which was of the order of several tens of nanometers, could be adjusted by the number of successive deposition cycles, the functionality of the embedded inorganic nanoparticles was preserved [237]. The wall thicknesses of the nanotubes reported in this study were only slightly lager than those in smooth configurations, and the mechanical stability of the nanotubes depended on the number of bilayers their walls consisted of.

Layer-by-layer deposition into porous hard templates has meanwhile been extended to other polyelectrolyte pairs. For example, Ai et al. prepared polypyrrole/poly(allylamine hydrochloride) nanotubes consisting of six or 12 bilayers in PC membranes with a D_p-value of 400 nm that had initially been coated with poly(ethylenimine) [238]. Again, the observed value of the wall thickness of the nanotubes of some tens of nanometers was much larger than that of corresponding multilayer systems deposited on smooth substrates. However, a clear dependence of the wall thickness on the number of deposition cycles was found. Nanotubes consisting of dendrimers were fabricated by Kim and coworkers (Fig. 29a) [239]. Dendrimers, synthesized by stepwisely attaching another generation of low-molar mass building blocks to a parent structure, represent a class of functional materials which can be customized with an unrivaled precision. On the one hand, they can be employed as functional nanocontainers. On the other hand, they contain a well-defined number of terminal functional groups residing at their surface [240–242]. For the preparation of the dendrimer nanotubes, bilayers containing globular-shaped, N,N-disubstituted hydrazine phosphorus-containing dendrimers [243] of the fourth generation having 96 terminal functional groups with either cationic $[G_4(NH^+Et_2Cl^-)_{96}]$ or anionic $[G_4(CH-COO^-Na^+)_{96}]$
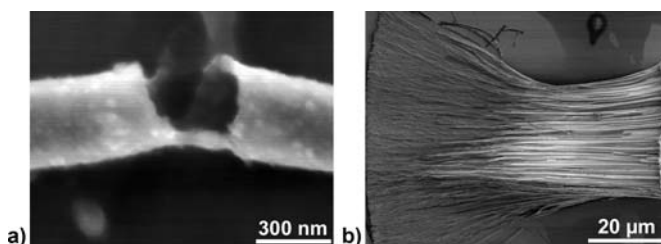
Fig. 29 SEM images of dendrimer nanotubes obtained by layer-by-layer deposition. **a** Broken nanotube; **b** array consisting of nanotubes exhibiting a gradient of their mechanical stability along their long axes. Reproduced from [239]. © (2005) Wiley-VCH

character were deposited on the walls of AAO hard templates with a D_p-value of 400 nm. Since dendrimers can be considered as hard spheres, nanotubes consisting of dendrimeric polyelectrolytes might be useful if swelling or deswelling needs to be minimized. The mechanical stability of the dendrimer nanotubes increased with the number of deposited bilayers. In the case of dendrimer nanotubes with high aspect ratios of the order of 200 that were prepared in hard templates with closed pore bottoms, their mechanical stability decreased with increasing distance to the pore opening. Whereas the nanotube segments initially located next to the pore openings with a length of about 35 μm were rigid, the nanotube segments farther away from the pore openings were prone to mechanical deformation due to the occurrence of capillary forces, which occur when nanofiber arrays dry after the wet-chemical etching of the hard template (Fig. 29b). Lu et al. reported the deposition of the hemoprotein human serum albumin (HSA) into AAO hard templates with a D_p-value of about 200 nm [244, 245]. Inversion of the charges borne by the HSA molecules was achieved by adjusting the pH-value of the solutions used for deposition to values below or above the isoelectric point of HSA. Therefore, in alternating deposition steps HSA could be deposited as a polycation or as a polyanion. Moreover, nanotubes whose walls consisted of HSA/phospholipid multilayers were prepared [244].

Extending the initial approach to exploit electrostatic interactions between polyelectrolytic building blocks for their rational arrangement in nanotube walls by layer-by-layer assembly, a number of modifications of this methodology based on different kinds of interactions have been developed. For example, the formation of hydrogen bonds between hydroxyl groups of poly(acrylic acid) and the nitrogen groups of poly(4-vinylpyridine) was exploited to coat the pore walls of PC membranes with multilayer structures consisting of these polyelectrolytes [246]. An advantage of this approach lies in the fact that solutions in organic solvents can be used to deposit the monolayers. Nanotubes consisting of poly(ethylenimine)/poly(styrene-*alt*-maleic anhydride) multilayers were obtained by connecting the alternating monolayers by amide bonds [247]. A similar approach was applied to incorporate

the fluorescent compound 3,4,9,10-perylenetetracarboxylicdianhydride into nanotubes having multilayered walls with poly(ethylenimine) as a second component [248]. Since the fluorescent component retained its fluorescence, single nanotubes could be imaged by fluorescence microscopy, and the formation of the multilayer structure could be monitored by UV absorption spectroscopy. It was found that the absorption linearly increased along with the number of deposition cycles.

Hou et al. reported the fabrication of glutaraldehyde/protein nanotubes [249]. Using phosphorous-containing coupling agents, a first glutaraldehyde layer was grafted onto the pore walls of AAO hard templates with a D_p-value of 200 nm. Subsequently, a protein layer was bonded with its free amino sites to the excess aldehyde functions of the glutaraldehyde layer, and in turn another glutaraldehyde layer to free amino sites of the proteins. For example, bioactive nanotubes could be fabricated by the repeated deposition of glutaraldehyde/glucose oxidase bilayers. The activity of the glucose oxidase in the liberated nanotubes increased along with the number of protein layers in their walls. However, inside the AAO hard templates the activity of the nanotubes decreased for more than three bilayers, because the accessibility of the protein molecules through the hollow channel inside the nanotubes became more and more limited as the diameter of the channel decreased with each additional layer. Also, Hou et al. showed that hemoglobin nanotubes that were produced in a similar manner exhibited heme electroactivity. Tian et al. used AAO hard templates activated with a poly(ethylenimine)/poly(sodium-4-styrenesulfonate) bilayer to deposit cytochrome C/glutaraldehyde bilayers and obtained nanotubes in which the bioactivity and the electronic properties of cytochrome C were retained [250]. Hou et al. fabricated DNA nanotubes employing a hybridization-based layer-by-layer strategy. After the initial grafting of DNA strands on the pore walls with the aid of phosphorous-containing coupling agents, the hard templates were successively immersed into DNA solutions, allowing binding of further DNA strands to those already immobilized by hybridization [251].

Whereas layer-by-layer deposition into porous hard templates has been proven to be a promising access to precisely designed polymeric nanotubes that can functionalize hard templates or that can be released, two problems still need to be addressed. The first one is elucidating the structure formation of the polyelectrolyte layers inside hard templates. The significantly increased thickness of bilayers reported by Ai et al. [236] was also observed by other authors. Lee et al. found that the thickness of poly(allylamine hydrochloride)/poly(sodium-4-styrenesulfonate) multilayers deposited into porous PC membranes exceeded that of corresponding multilayers on smooth substrates obtained after the same number of deposition cycles. For example, 24.5 bilayers had a thickness of 250 nm within a hard template as compared to 155 nm on a smooth silicon wafer [252]. Alem et al. studied the layer-by-layer deposition of a pair of strong polyelectrolytes, namely

poly(vinylbenzylammonium chloride) as a polycation and poly(sodium-4-styrenesulfonate) as a polyanion, into track-etched PC membranes with D_p-values ranging from 50 to 850 nm. The end-to-end distances of the polyelectrolyte chains were systematically varied by varying the molecular weight and the ionic strength of the solutions used for deposition [253]. Whereas the bilayers deposited on smooth substrates had a thickness of 1–3 nm, the first bilayer deposited into porous hard templates covering the pore walls had a thickness of 50–120 nm. Further deposition cycles led to only small increases in the thickness of the polyelectrolyte layers, which turned out to be nearly independent of the end-to-end distance of the polyelectrolytes and the ionic strength of the stock solutions used but strongly depended on the D_p-values of the hard templates. For small D_p-values, the thickness of the polyelectrolyte layers was proportional to D_p, whereas progressive deviations from this relationship were found for D_p-values larger than 250 nm. On the basis of geometric considerations, Alem et al. proposed a mechanism governing the growth of polyelectrolyte layers inside porous hard templates that involves the enrichment of the polyelectrolytes inside the pores. Hence, a dense, swollen polyelectrolyte gel fills pores and collapses upon drying.

The second issue that needs to be further addressed is the development of strategies for the anchoring of the first deposited layer onto the pore walls of the hard templates. This is particularly the case for the widely used AAO membranes, whose pore walls consist of amorphous alumina containing water, electrolyte anions and positively charged defects (Sect. 2). Moreover, composition and distribution of the contaminations across the pore walls are inhomogeneous (see, for example, [30–32]). Therefore, isotropic etching steps performed to widen the pores of as-anodized, self-ordered AAO with an initial porosity of 10% [40] or below will change the properties of the pore walls and affect their reactivity. In the case of commercially available disordered AAO membranes with a D_p-value of 200 nm positively charged polyelectrolytes such as poly(ethylenimine) [247, 250] or human serum albumin at a pH value of 3.8 [244] could directly be deposited as the first layer. However, Dai et al. reported a procedure to coat the same type of hard templates that started with the deposition of poly(acrylic acid), hence with a polyanion, at a pH value of 4.0 [254]. The reports dealing with the surface chemistry of AAO are to a large extent inconsistent, and it appears that the surface properties of the pore walls largely depend on the anodization conditions and post-anodization treatments. Strategies to overcome the problems associated with the lack of knowledge of the properties of the hard templates are based on their modification by grafting anchor layers onto the pore walls. For example, Kim et al. used 3-aminopropyl-dimethylethoxysilane, a silane coupling agent, to generate a layer with a high density of positive charges on the walls of self-ordered porous alumina with a D_p-value of 400 nm [239]. Hou et al. [249, 251, 255] adapted a surface modification strategy based on a double layer of phosphorous-containing coupling agents initially introduced

by Mallouk and coworkers [256] that allowed further layer-by-layer deposition mediated by specific chemical interactions.

First applications of polymeric nanotubes fabricated by layer-by-layer deposition have already been reported. Using track-etched PC membranes with D_p-values ranging from 400 to 800 nm functionalized with poly(allylamine hydrochloride)/poly(sodium-4-styrenesulfonate) bilayers, Lee et al. demonstrated reversible pH-induced hysteretic gating [252]. Membrane pores, the walls of which were covered with 18.5 bilayers, could be closed to a pH-value of 2.5 by swelling the polyelectrolytes. The pores thus closed retained their closed state up to pH 9. At higher pH values, the swollen polyelectrolyte layer collapsed, and the pores switched to the open state. The switching behavior of the system could be customized by the number of bilayers deposited on the pore walls. The flux of pH-adjusted water through membrane was studied and indicated discontinuous swelling/deswelling behavior (Fig. 30) but lesser swelling in pores than on smooth substrates (Fig. 31). Lee et al. suggested that swelling in the pores of hard templates is suppressed because of the curvature-induced stress generated by the volume expansion in a curved geometry.

Dai et al. reported a strategy for analyzing proteins by selective binding to antibodies in such a way that nonspecific adsorption and protein denaturation could be prevented. To this end, poly(acrylic acid)/protonated poly(allylamine) multilayers that are well known to resist nonspecific adsorption of proteins and to allow for covalent immobilization of arrays of active antibodies were coated on the walls of AAO hard templates with
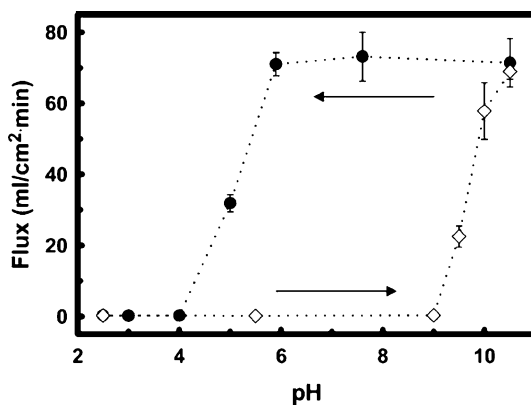

Fig. 30 Reversible pH-induced hysteretic gating with layer-by-layer nanotubes. Changes in flux through a membrane functionalized with poly(allylamine hydrochloride)/poly(sodium-4-styrenesulfonate) nanotubes as a function of pH. The *filled circles* and *open diamonds* represent data generated after a pH 10.5 pretreatment and after a pH 2.5 pretreatment, respectively. *Error bars* represent standard deviations. Reproduced from [252]. © (2006) American Chemical Society
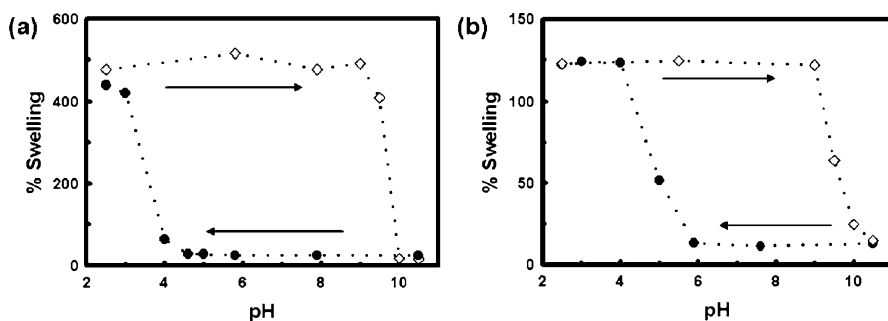
Fig. 31 Comparison of the swelling ratio of poly(allylamine hydrochloride)/poly(sodium-4-styrenesulfonate) multilayers **a** on a planar Si substrate (determined by in-situ ellipsometry) and **b** in the cylindrical pores of a 800 nm pore track-etched PC membrane. The *filled circles* and *open diamonds* represent data generated after a pH 10.5 pretreatment and after a pH 2.5 pretreatment, respectively. Reproduced from [252]. © (2006) American Chemical Society

a D_p-value of 200 nm. Activation of the surface carboxyl groups of the poly(acrylic acid) with N-(3-dimethylaminopropyl)-N'-ethylcarbodiimide and N-hydroxysuccinimide enabled the covalent attachment of antibodies. A 500-fold increase in the surface area as compared to thin film configurations decreased the protein-microarray detection limit by two orders of magnitude [254]. Feng et al. adapted the procedure for the fabrication of dendrimer nanotubes reported by Kim et al. [239] to incorporate a graded bandgap structure similar to that previously reported by Franzl et al. for thin-film configurations on smooth substrates [257] into the walls of dendrimer nanotubes. The dendrimer layers acted as a rigid scaffold for the engineering of a multilayer configuration of inorganic semiconductor quantum dots having different diameters. Taking advantage of a fluorescence resonance energy transfer cascade from donor nanoparticles located near the outer surface on the nanotube walls to acceptor particles located near the inner surface of the nanotube walls, the hybridization of DNA strands grafted on the inner tube surface with complementary labeled DNA strands could be detected with significantly increased sensitivity [258].

7
Conclusion

One-dimensional polymeric nanostructures or one-dimensional nanostructures derived from polymeric soft templates are being considered as functional building blocks for a broad range of device architectures, and some promising applications have already been reported. Various well-established approaches allow forming virtually any functional material into a tubular or

a solid rod-like shape. This review is based on the paradigm that the control over their internal mesoscopic fine structure is the most crucial means of tailoring the properties of one-dimensional nanoobjects, whereas the presence or absence of a central hollow space and therefore the distinction between "tubes" and "solid rods" is, in many cases, of minor importance. This is all the more the case for polymeric nanotubes and nanorods as the supramolecular organization on mesoscopic length scales determines the properties of polymeric materials to a large extent. Nanoporous, shape-defining hard templates provide a two-dimensionally confined space in which self-organization processes such as crystallization, mesophase formation, and phase separation may result in supramolecular fine structures fundamentally different from those obtained in thin film configurations and in the bulk. A particular advantage of hard templates is the possibility to induce and manipulate self-assembly inside the shape-defining pores. Therefore, many more parameters allow tailoring of the mesoscopic morphology of the nanofibers in hard-template-based preparation processes than in procedures for their production not relying on the rigidity of confining pore walls. The supramolecular organization in the two-dimensional confinement of nanopores can be manipulated by the pore diameter, the nature of the pore walls, the composition of the infiltrated material, environmental conditions, and the thermal history of the sample. Moreover, nanotubes characterized by complex, multilayered walls are accessible by successive deposition steps into the hard templates, thus exploiting specific interactions between the deposited species and the material already deposited. Thus, by the preparative approaches reviewed in this contribution complex functional supramolecular structures can be generated in one-dimensional nanofibers. Examples for this are ordered mesoporous structures and microphase morphologies, uniform crystalline and liquid crystalline textures, as well as the incorporation of inorganic nanoparticles into the walls of polymer nanotubes. The control over the supramolecular organization of the materials the nanotubes consist of is the prerequisite for the rational tailoring of peculiar mechanical, optical and electronic properties.

Even though first applications for nanotubes with walls exhibiting a customized supramolecular organization have been demonstrated, the understanding of and the control over the relevant structure formation processes involving polymeric materials confined to hard templates need to be improved. Promising configurations for device components are, on the one hand, composite membranes consisting of the hard template and the nanotubes inside their pores, which are of potential interest for applications in the fields of storage, separation and catalysis. On the other hand, arrays of released nanofibers may have specific adhesive and wetting properties or can be used as nanosensor and nanoactuator arrays. However, the up-scaling of the production of such nanofiber assemblies requires their destruction-free removal from recyclable hard templates. To create nanofiber arrays usable in

real life applications, their mechanical stability has to be improved and condensation of the nanofibers has to be prevented by optimizing the geometry of the array.

References

1. Bognitzki M, Hou HQ, Ishaque M, Frese T, Hellwig M, Schwarte C, Schaper A, Wendorff JH, Greiner A (2000) Adv Mater 12:637
2. Wehrspohn RB (2005) Ordered porous nanostructures and applications. Springer, Berlin Heidelberg New York
3. Martin CR (1994) Science 266:1961
4. Martin CR (1996) Chem Mater 8:1739
5. Huczko A (2000) Appl Phys A 70:365
6. Cai ZH, Martin CR (1989) J Am Chem Soc 111:4138
7. Liang WB, Martin CR (1990) J Am Chem Soc 112:9666
8. Martin CR, Vandyke LS, Cai ZH, Liang WB (1990) J Am Chem Soc 112:8976
9. Martin CR (1991) Adv Mater 3:457
10. Parthasarathy RV, Martin CR (1994) Chem Mater 6:1627
11. Martin CR (1995) Acc Chem Res 28:61
12. Menon VP, Lei JT, Martin CR (1996) Chem Mater 8:2382
13. Cepak VM, Martin CR (1999) Chem Mater 11:1363
14. Penner RM, Martin CR (1986) J Electrochem Soc 133:2206
15. Kohli P, Harrell CC, Cao ZH, Gasparac R, Tan WH, Martin CR (2004) Science 305:984
16. Lakshmi BB, Martin CR (1997) Nature 388:758
17. Jin MH, Feng XJ, Feng L, Sun TL, Zhai J, Li TJ, Jiang L (2005) Adv Mater 17:1977
18. Xu JH, Li M, Zhao Y, Lu QH (2007) Coll Surf A 302:136
19. Chen X, Steinhart M, Hess C, Gösele U (2006) Adv Mater 18:2153
20. Grimm S, Schwirn K, Göring P, Knoll H, Miclea PT, Greiner A, Wendorff JH, Wehrspohn RB, Gösele U, Steinhart M (2007) Small 3:993
21. Ott AW, Klaus JW, Johnson JM, George SM, McCarley KC, Way JD (1997) Chem Mater 9:707
22. Xiong G, Elam JW, Feng H, Han CY, Wang HH, Iton LE, Curtiss LA, Pellin MJ, Kung M, Kung H, Stair PC (2005) J Phys Chem B 109:14059
23. Apel P (2001) Radiation Measurements 34:559
24. Crawford GP, Steele LM, Ondriscrawford R, Iannacchione GS, Yeager CJ, Doane JW, Finotello D (1992) J Chem Phys 96:7788
25. Diggle JW, Downie TC, Goulding CW (1969) Chem Rev 69:365
26. O'Sullivan JP, Wood GC (1970) Proc Royal Soc London Ser A 317:511
27. Keller F, Hunter MS, Robinson DL (1953) J Electrochem Soc 100:411
28. Thompson GE, Wood GC (1981) Nature 290:230
29. Thompson GE, Furneaux RC, Wood GC, Richardson JA, Goode JS (1978) Nature 272:433
30. Chen W, Yuan JH, Xia XH (2005) Anal Chem 77:8102
31. Choi J, Luo Y, Wehrspohn RB, Hillebrand R, Schilling J, Gösele U (2003) J Appl Phys 94:4757

32. Vrublevsky I, Jagminas A, Schreckenbach J, Goedel WA (2007) Appl Surf Sci 253:4680
33. Zhao L, Yosef M, Pippel E, Hofmeister H, Steinhart M, Gösele U, Schlecht S (2006) Angew Chem Int Ed 45:8042
34. Zhao LL, Yosef M, Steinhart M, Göring P, Hofmeister H, Gösele U, Schlecht S (2006) Angew Chem Int Ed 45:311
35. Wang Y, Wu K (2005) J Am Chem Soc 127:9686
36. Masuda H, Fukuda K (1995) Science 268:1466
37. Masuda H, Hasegwa F, Ono S (1997) J Electrochem Soc 144:L127
38. Masuda H, Yada K, Osaka A (1998) Japan J Appl Phys Part 2 37:L1340
39. Li AP, Müller F, Birner A, Nielsch K, Gösele U (1998) J Appl Phys 84:6023
40. Nielsch K, Choi J, Schwirn K, Wehrspohn RB, Gösele U (2002) Nano Lett 2:677
41. Lee W, Ji R, Gösele U, Nielsch K (2006) Nat Mater 5:741
42. Chu SZ, Wada K, Inoue S, Isogai M, Yasumori A (2005) Adv Mater 17:2115
43. Masuda H, Takenaka K, Ishii T, Nishio K (2006) Jpn J Appl Phys 2-Letters & Express Lett 45: L1165
44. Masuda H, Nagae M, Morikawa T, Nishio K (2006) Jpn J Appl Phys 2-Letters & Express Lett 45: L406
45. Masuda H, Yamada H, Satoh M, Asoh H, Nakao M, Tamamura T, Ye (1997) Appl Phys Lett 71:2770
46. Choi J, Nielsch K, Reiche M, Wehrspohn RB, Gösele U (2003) J Vacuum Sci Technol B 21:763
47. Lee W, Ji R, Ross CA, Gösele U, Nielsch K (2006) Small 2:978
48. Berg JC (1993) Wettability. Dekker, New York
49. Fox HW, Hare EF, Zisman WA (1955) J Phys Chem 59:1097
50. De Gennes PG (1985) Rev Modern Phys 57:827
51. Ausserré D, Picard AM, Léger L (1986) Phys Rev Lett 57:2671
52. Léger L, Joanny JF (1992) Reports Progr Phys 55:431
53. Derjaguin BV, Churaev NV (1974) J Coll Inter Sci 49:249
54. Mate CM, Novotny VJ (1991) J Chem Phys 94:8420
55. Israelachvili JN (1991) Intermolecular and surface forces. Academic Press, New York
56. Bernadiner MG (1998) Transport in Porous Media 30:251
57. Everett DH, Haynes JM (1972) J Coll Inter Sci 38:125
58. Hammond PS (1983) J Fluid Mechanics 137:363
59. Lenormand R (1990) J Phys-Condens Matter 2:SA79
60. Steinhart M, Wendorff JH, Greiner A, Wehrspohn RB, Nielsch K, Schilling J, Choi J, Gösele U (2002) Science 296:1997
61. Zhang MF, Dobriyal P, Chen JT, Russell TP, Olmo J, Merry A (2006) Nano Lett 6:1075
62. Steinhart M, Wendorff JH, Wehrspohn RB (2003) Chem Phys Chem 4:1171
63. Steinhart M, Wehrspohn RB, Gösele U, Wendorff JH (2004) Angew Chem Int Ed 43:1334
64. Steinhart M, Göring P, Dernaika H, Prabhukaran M, Gösele U, Hempel E, Thurn-Albrecht T (2006) Phys Rev Lett 97:027801
65. Steinhart M, Murano S, Schaper AK, Ogawa T, Tsuji M, Gösele U, Weder C, Wendorff JH (2005) Adv Functional Mater 15:1656
66. Lau S, Zheng RK, Chan HLW, Choy CL (2006) Mater Lett 60:2357
67. Zheng RK, Yang Y, Wang Y, Wang J, Chan HLW, Choy CL, Jin CG, Li XG (2005) Chem Commun, p 1447
68. She XL, Song GJ, Li JJ, Han P, Yang SJ, Peng Z (2006) J Mater Res 21:1209
69. She XL, Song GJ, Li JJ, Han P, Yang SJ, Wang SL, Peng Z (2006) Polym J 38:639
70. Kim E, Xia YN, Whitesides GM (1995) Nature 376:581

71. Suh KY, Kim YS, Lee HH (2001) Adv Mater 13:1386
72. Moon SI, McCarthy TJ (2003) Macromolecules 36:4253
73. Kriha O, Zhao LL, Pippel E, Gösele U, Wehrspohn RB, Wendorff JH, Steinhart M, Greiner A (2007) Adv Functional Mater 17:1327
74. Xiang HQ, Shin K, Kim T, Moon SI, McCarthy TJ, Russell TP (2004) Macromolecules 37:5660
75. Sun YM, Steinhart M, Zschech D, Adhikari R, Michler GH, Gösele U (2005) Macromolecular Rapid Commun 26:369
76. Shin K, Obukhov S, Chen J-T, Huh J, Hwang Y, Mok S, Dobriyal P, Thiyagarajan P, Russell TP (2007) Nat Mater 6:961
77. Song GJ, She XL, Fu ZF, Li JJ (2004) J Mater Res 19:3324
78. Li JJ, Song GJ, She XL, Han P, Peng Z, Chen D (2006) Polymer J 38:554
79. Steinhart M, Senz S, Wehrspohn RB, Gösele U, Wendorff JH (2003) Macromolecules 36:3646
80. Primak SV, Jin T, Dagger AC, Finotello D, Mann EK (2002) Phys Rev E 65:031804
81. Ai SF, Cui Y, He Q, Tao C, Li JB (2006) Colloid Surface A 275:218
82. Binder K (1998) J Non-Equil Thermod 23:1
83. Gelb LD, Gubbins KE, Radhakrishnan R, Sliwinska-Bartkowiak M (1999) Rep Prog Phys 62:1573
84. Liu AJ, Durian DJ, Herbolzheimer E, Safran SA (1990) Phys Rev Lett 65:1897
85. Steinhart M, Jia ZH, Schaper AK, Wehrspohn RB, Gösele U, Wendorff JH (2003) Adv Mater 15:706
86. De Gennes PG (1981) Macromolecules 14:1637
87. Lai PY, Binder K (1992) J Chem Phys 97:586
88. O'Shaughnessy B, Vavylonis D (2005) J Phys-Condens Matter 17:R63
89. Chen JT, Shin K, Leiston-Belanger JM, Zhang MF, Russell TP (2006) Adv Functional Mater 16:1476
90. Rodriguez AT, Chen M, Chen Z, Brinker CJ, Fan HY (2006) J Am Chem Soc 128:9276
91. Gonuguntla M, Sharma A (2004) Langmuir 20:3456
92. Rayleigh L (1892) Philosophical Magazine Serié 5 34:177
93. Quere D, Dimeglio JM, Brochard-Wyart F (1990) Science 249:1256
94. Chen JT, Zhang MF, Russell TP (2007) Nano Letters 7:183
95. Sirringhaus H, Brown PJ, Friend RH, Nielsen MM, Bechgaard K, Langeveld-Voss BMW, Spiering AJH, Janssen RAJ, Meijer EW, Herwig P, de Leeuw DM (1999) Nature 401:685
96. Lovinger AJ (1983) Science 220:1115
97. Kepler RG, Anderson RA (1978) J Appl Phys 49:1232
98. Dveyaharon H, Sluckin TJ, Taylor PL, Hopfinger AJ (1980) Phys Rev B 21:3700
99. Broadhurst MG, Davis GT (1981) Ferroelectrics 32:177
100. Shin K, Woo E, Jeong YG, Kim C, Huh J, Kim KW (2007) Macromolecules 40:6617
101. Wu H, Wang W, Yang HX, Su ZH (2007) Macromolecules 40:4244
102. Zhi LJ, Gorelik T, Wu JS, Kolb U, Müllen K (2005) J Am Chem Soc 127:12792
103. Zhi LJ, Wu JS, Li JX, Kolb U, Müllen K (2005) Angew Chem Int Ed 44:2120
104. Woo E, Huh J, Jeong YG, Shin K (2007) Phys Rev Lett 98:136103
105. Koenig JL (1999) Spectroscopy of polymers. Elsevier, Amsterdam
106. Martin CR, Parthasarathy R, Menon V (1993) Synthetic Metals 55:1165
107. Cai ZH, Lei JT, Liang WB, Menon V, Martin CR (1991) Chem Mater 3:960
108. Keller A (1957) Philosophical Magazine 2:1171
109. Reiter G, Strobl GR (2007) Progress in understanding of polymer crystallization. Springer, Berlin Heidelberg New York

110. Strobl GR (2007) The physics of polymers: concepts for understanding their structures and behavior. Springer, Berlin Heidelberg New York
111. Keith HD, Padden FJ (1963) J Appl Phys 34:2409
112. Bassett DC, Vaughan AS (1985) Polymer 26:717
113. Granasy L, Pusztai T, Tegze G, Warren JA, Douglas JF (2005) Phys Rev E 72:011605
114. Turnbull D (1950) J Appl Phys 21:1022
115. Turnbull D (1950) Journal of Chemical Physics 18:198
116. O'Carroll D, Lieberwirth I, Redmond G (2007) Small 3:1178
117. Quiram DJ, Register RA, Marchand GR, Adamson DH (1998) Macromolecules 31:4891
118. Loo YL, Register RA, Ryan AJ (2000) Phys Rev Lett 84:4120
119. Zhu L, Cheng SZD, Calhoun BH, Ge Q, Quirk RP, Thomas EL, Hsiao BS, Yeh FJ, Lotz B (2000) J Am Chem Soc 122:5957
120. Loo YL, Register RA, Ryan AJ, Dee GT (2001) Macromolecules 34:8968
121. Reiter G, Castelein G, Sommer JU, Röttele A, Thurn-Albrecht T (2001) Phys Rev Lett 8722:226101
122. Beiner M, Rengarajan GT, Pankaj S, Enke D, Steinhart M (2007) Nano Lett 7:1381
123. Zhao LL, Lu TZ, Yosef M, Steinhart M, Zacharias M, Gösele U, Schlecht S (2006) Chem Mater 18:6094
124. Laschat S, Baro A, Steinke N, Giesselmann F, Hagele C, Scalia G, Judele R, Kapatsina E, Sauer S, Schreivogel A, Tosoni M (2007) Angew Chem Int Ed 46:4832
125. Pisula W, Tomovic Z, El Hamaoui B, Watson MD, Pakula T, Müllen K (2005) Adv Functional Mater 15:893
126. Wu JS, Pisula W, Müllen K (2007) Chem Rev 107:718
127. Pisula W, Kastler M, Wasserfallen D, Davies RJ, Garcia-Gutierrez MC, Müllen K (2006) J Am Chem Soc 128:14424
128. Kastler M, Pisula W, Davies RJ, Gorelik T, Kolb U, Müllen K (2007) Small 3:1438
129. Zhi LJ, Wu JS, Li JX, Stepputat M, Kolb U, Müllen K (2005) Adv Mater 17:1492
130. Liu QY, Li Y, Liu HG, Chen YL, Wang XY, Zhang YX, Li XY, Jiang JZ (2007) J Phys Chem C 111:7298
131. Barrett C, Iacopino D, O'Carroll D, De Marzi G, Tanner DA, Quinn AJ, Redmond G (2007) Chem Mater 19:338
132. Palermo V, Liscio A, Talarico AM, Zhi LJ, Mullen K, Samori P (2007) Philos T Roy Soc A 365:1577
133. Enke D, Janowski F, Schwieger W (2003) Micropor Mesopor Mater 60:19
134. Bognitzki M, Czado W, Frese T, Schaper A, Hellwig M, Steinhart M, Greiner A, Wendorff JH (2001) Adv Mater 13:70
135. Bognitzki M, Frese T, Steinhart M, Greiner A, Wendorff JH, Schaper A, Hellwig M (2001) Poly Eng Sci 41:982
136. Greiner A, Wendorff JH (2007) Angew Chem Int Ed 46:5670
137. Cahn JW (1961) Acta Metallurgica 9:795
138. Hashimoto T (1993) In: Thomas EL (ed) Structure and Properties of Polymers (Materials Science and Technology), vol 12. Wiley, Weinheim, p 251
139. De Gennes PG (1980) J Chem Phys 72:4756
140. Jones RAL, Norton LJ, Kramer EJ, Bates FS, Wiltzius P (1991) Phys Rev Lett 66:1326
141. Krausch G, Dai CA, Kramer EJ, Bates FS (1994) Berichte Der Bunsen-Gesellschaft-Physical Chemistry Chemical Physics 98:446
142. Sung L, Karim A, Douglas JF, Han CC (1996) Phys Rev Lett 76:4368
143. Albano EV, Binder K, Heermann DW, Paul W (1992) Physica A 183:130
144. Gelb LD, Gubbins KE (1997) Phys Rev E 55:R1290

145. Gelb LD, Gubbins KE (1997) Phys Rev E 56:3185
146. Gelb LD, Gubbins KE (1997) Physica A 244:112
147. Luo Y, Lee SK, Hofmeister H, Steinhart M, Gösele U (2004) Nano Lett 4:143
148. Nielsch K, Castano FJ, Ross CA, Krishnan R (2005) J Appl Phys 98:6
149. Nielsch K, Castano FJ, Matthias S, Lee W, Ross CA (2005) Adv Eng Mater 7:217
150. Tanaka K, Takahara A, Kajiyama T (1998) Macromolecules 31:863
151. Tanaka K, Kajiyama T, Takahara A, Tasaki S (2002) Macromolecules 35:4702
152. Walheim S, Böltau M, Mlynek J, Krausch G, Steiner U (1997) Macromolecules 30:4995
153. Buck E, Fuhrmann J (2001) Macromolecules 34:2172
154. Harris M, Appel G, Ade H (2003) Macromolecules 36:3307
155. Kresge CT, Leonowicz ME, Roth WJ, Vartuli JC, Beck JS (1992) Nature 359:710
156. Attard GS, Glyde JC, Göltner CG (1995) Nature 378:366
157. Lu YF, Ganguli R, Drewien CA, Anderson MT, Brinker CJ, Gong WL, Guo YX, Soyez H, Dunn B, Huang MH, Zink JI (1997) Nature 389:364
158. Templin M, Franck A, DuChesne A, Leist H, Zhang YM, Ulrich R, Schädler V, Wiesner U (1997) Science 278:1795
159. Zhao DY, Feng JL, Huo QS, Melosh N, Fredrickson GH, Chmelka BF, Stucky GD (1998) Science 279:548
160. Joo SH, Choi SJ, Oh I, Kwak J, Liu Z, Terasaki O, Ryoo R (2001) Nature 412:169
161. Ryoo R, Joo SH, Kruk M, Jaroniec M (2001) Adv Mater 13:677
162. Liang CD, Hong KL, Guiochon GA, Mays JW, Dai S (2004) Angew Chem Int Ed 43:5785
163. Zhang FQ, Meng Y, Gu D, Yan Y, Yu CZ, Tu B, Zhao DY (2005) J Am Chem Soc 127:13508
164. Liang CD, Dai S (2006) J Am Chem Soc 128:5316
165. Zhang FQ, Gu D, Yu T, Zhang F, Xie SH, Zhang LJ, Deng YH, Wan Y, Tu B, Zhao DY (2007) J Am Chem Soc 129:7746
166. Ying JY, Mehnert CP, Wong MS (1999) Angew Chem Int Ed 38:56
167. Davis ME (2002) Nature 417:813
168. Kickelbick G (2005) Small 1:168
169. Lu AH, Schüth F (2006) Adv Mater 18:1793
170. Kanatzidis MG (2007) Adv Mater 19:1165
171. Wan Y, Shi YF, Zhao DY (2007) Chem Comm: 897
172. Wan Y, Zhao DY (2007) Chem Rev 107:2821
173. Yang ZL, Niu ZW, Cao XY, Yang ZZ, Lu YF, Hu ZB, Han CC (2003) Angew Chem Int Ed 42:4201
174. Liang ZJ, Susha AS (2004) Chem-Eur J 10:4910
175. Yao B, Fleming D, Morris MA, Lawrence SE (2004) Chem Mater 16:4851
176. Zhu WP, Han YC, An LJ (2005) Micropor Mesopor Mater 84:69
177. Chae WS, Lee SW, An MJ, Choi KH, Moon SW, Zin WC, Jung JS, Kim YR (2005) Chem Mater 17:5651
178. Lu QY, Gao F, Komarneni S, Mallouk TE (2004) J Am Chem Soc 126:8650
179. Wang DH, Kou R, Yang ZL, He JB, Yang ZZ, Lu YF (2005) Chem Commun, p 166
180. Platschek B, Petkov N, Bein T (2006) Angew Chem Int Ed 45:1134
181. Jin KW, Yao BD, Wang N (2005) Chem Phys Lett 409:172
182. Wu YY, Cheng GS, Katsov K, Sides SW, Wang JF, Tang J, Fredrickson GH, Moskovits M, Stucky GD (2004) Nat Mater 3:816
183. Wu YY, Livneh T, Zhang YX, Cheng GS, Wang JF, Tang J, Moskovits M, Stucky GD (2004) Nano Lett 4:2337

184. Yu K, Hurd AJ, Eisenberg A, Brinker CJ (2001) Langmuir 17:7961
185. Chen X, Knez M, Berger A, Nielsch K, Gösele U, Steinhart M (2007) Angew Chem Int Ed 46:6829
186. Chae WS, Lee SW, Kim YR (2005) Chem Mater 17:3072
187. Wang K, Wei MD, Morris MA, Zhou HS, Holmes JD (2007) Adv Mater 19:3016
188. Cott DJ, Petkov N, Morris MA, Platschek B, Bein T, Holmes JD (2006) J Am Chem Soc 128:3920
189. Steinhart M, Liang CD, Lynn GW, Gösele U, Dai S (2007) Chem Mater 19:2383
190. Wang K, Zhang W, Phelan R, Morris MA, Holmes JD (2007) J Am Chem Soc 129:13388
191. Klotz M, Albouy PA, Ayral A, Menager C, Grosso D, Van der Lee A, Cabuil V, Babonneau F, Guizard C (2000) Chem Mater 12:1721
192. Grosso D, Balkenende AR, Albouy PA, Ayral A, Amenitsch H, Babonneau F (2001) Chem Mater 13:1848
193. Yamaguchi A, Uejo F, Yoda T, Uchida T, Tanamura Y, Yamashita T, Teramae N (2004) Nat Mater 3:337
194. Yoo SJ, Ford DM, Shantz DF (2006) Langmuir 22:1839
195. Abetz V, Simon PFW (2005) Block Copolymers I (Advances in Polymer Science), vol 189. Springer, Berlin Heidelberg New York, p 125
196. Bates FS, Fredrickson GH (1990) Annual Rev Phys Chem 41:525
197. Castelletto V, Hamley IW (2004) Curr Opin Solid State Mater Sci 8:426
198. Russell TP (1996) Curr Opin Colloid In 1:107
199. Fasolka MJ, Mayes AM (2001) Annual Rev Mater Res 31:323
200. Chen P, Liang HJ, Shi AC, Yp (2007) Macromolecules 40:7329
201. Li WH, Wickham RA (2006) Macromolecules 39:8492
202. Li WH, Wickham RA, Garbary RA (2006) Macromolecules 39:806
203. Miao B, Yan DD, Wickham RA, Shi AC (2007) Polymer 48:4278
204. Sevink GJA, Zvelindovsky AV, Fraaije J, Huinink HP, Qu (2001) J Chem Phys 115:8226
205. Feng J, Liu HL, Hu Y (2006) Macromol Theor Simul 15:674
206. Xu JB, Wu H, Lu DY, He XF, Zhao YH, Wen H (2006) Molec Simul 32:357
207. He XH, Song M, Liang HJ, Pan CY, Qr (2001) J Chem Phys 114:10510
208. Wang Q (2007) J Chem Phys 126:024903
209. Feng J, Ruckenstein E (2006) Macromolecules 39:4899
210. Chen P, He XH, Liang HJ (2006) J Chem Phys 124:104906
211. Feng J, Ruckenstein E (2006) J Chem Phys 125:164911
212. Yu B, Sun PC, Chen TH, Jin QH, Ding DT, Li BH, Shi AC, Kz (2007) J Chem Phys 127:114906
213. Yu B, Sun PC, Chen TC, Jin QH, Ding DT, Li BH, Shi AC (2006) Phys Rev Lett 96:138306
214. Feng J, Ruckenstein E (2007) J Chem Phys 126:124902
215. Xiao XQ, Huang YM, Liu HL, Hu Y (2007) Macromol Theor Simul 16:166
216. Zhu YT, Jiang W (2007) Macromolecules 40:2872
217. Yu B, Sun PC, Chen TH, Jin QH, Ding DT, Li BH, Shi AC (2007) J Chem Phys 126:204903
218. Erukhimovich I, Johner A (2007) Epl 79:56004
219. Segalman RA, Yokoyama H, Kramer EJ, Jl (2001) Adv Mater 13:1152
220. Cheng JY, Mayes AM, Ross CA, Qa (2004) Nat Mat 3:823
221. Cheng JY, Ross CA, Smith HI, Thomas EL (2006) Adv Mater 18:2505
222. Xiang HQ, Shin K, Kim T, Moon S, McCarthy TJ, Russell TP (2005) J Poly Sci Pol Phys 43:3377

223. Shin K, Xiang HQ, Moon SI, Kim T, McCarthy TJ, Russell TP (2004) Science 306:76
224. Xiang H, Shin K, Kim T, Moon SI, McCarthy TJ, Russell TP (2005) Macromolecules 38:1055
225. Decher G, Hong JD (1991) Makromolekulare Chemie-Macromolecular Symposia 46:321
226. Lvov Y, Decher G, Möhwald H (1993) Langmuir 9:481
227. Decher G (1997) Science 277:1232
228. Feldheim DL, Grabar KC, Natan MJ, Mallouk TE, Vc (1996) J Am Chem Soc 118:7640
229. Schmitt J, Decher G, Dressick WJ, Brandow SL, Geer RE, Shashidhar R, Calvert JM, We (1997) Adv Mater 9:61
230. Caruso F, Lichtenfeld H, Giersig M, Möhwald H (1998) J Am Chem Soc 120:8523
231. Donath E, Sukhorukov GB, Caruso F, Davis SA, Möhwald H (1998) Angew Chem Int Ed Engl 37:2202
232. Caruso F, Caruso RA, Möhwald H (1998) Science 282:1111
233. Jiang CY, Tsukruk VV (2006) Adv Mater 18:829
234. Caruso F (2001) Adv Mater 13:11
235. Li JB, Cui Y (2006) J Nanosci Nanotechnol 6:1552
236. Ai SF, Lu G, He Q, Li JB (2003) J Am Chem Soc 125:11140
237. Liang ZJ, Susha AS, Yu AM, Caruso F (2003) Adv Mater 15:1849
238. Ai SF, He Q, Tao C, Zheng SP, Li JB (2005) Macromol Rapid Commu 26:1965
239. Kim DH, Karan P, Göring P, Leclaire J, Caminade AM, Majoral JP, Gösele U, Steinhart M, Knoll W (2005) Small 1:99
240. Frechet JMJ (1994) Science 263:1710
241. Tomalia DA, Naylor AM, Goddard WA (1990) Angew Chem Int Ed Engl 29:138
242. Bosman AW, Janssen HM, Meijer EW (1999) Chem Rev 99:1665
243. Majoral JP, Caminade AM (1999) Chem Rev 99:845
244. Lu G, Al SF, Li JB (2005) Langmuir 21:1679
245. Lu G, Komatsu T, Tsuchida E (2007) Chem Commun, p 2980
246. Tian Y, He Q, Cui Y, Tao C, Li JB (2006) Chem-Eur J 12:4808
247. Tian Y, He Q, Tao C, Cui Y, Ai S, Li JB (2006) J Nanosci Nanotechnol 6:2072
248. Tian Y, He Q, Tao C, Li JB (2006) Langmuir 22:360
249. Hou SF, Wang JH, Martin CR (2005) Nano Lett 5:231
250. Tian Y, He Q, Cui Y, Li JB (2006) Biomacromolecules 7:2539
251. Hou SF, Wang JH, Martin CR (2005) J Am Chem Soc 127:8586
252. Lee D, Nolte AJ, Kunz AL, Rubner MF, Cohen RE (2006) J Am Chem Soc 128:8521
253. Alem H, Blondeau F, Glinel K, Demoustier-Champagne S, Jonas AM (2007) Macromolecules 40:3366
254. Dai JH, Baker GL, Bruening ML (2006) Analyt Chem 78:135
255. Hou SF, Harrell CC, Trofin L, Kohli P, Martin CR (2004) J Am Chem Soc 126:5674
256. Lee H, Kepley LJ, Hong HG, Mallouk TE, L (1988) J Am Chem Soc 110:618
257. Franzl T, Klar TA, Schietinger S, Rogach AL, Feldmann J, Op (2004) Nano Lett 4:1599
258. Feng CL, Zhong XH, Steinhart M, Caminade AM, Majoral JP, Knoll W (2007) Adv Mater 19:1933